Combined Feedback and LIDAR-Based Feedforward Active Load Alleviation

Nicolas Fezans[*] and Hans-Dieter Joos[†]

This paper presents a combined feedback and feedforward active load alleviation system and its associated design and tuning methodology. The feedback part is strongly structured and its robust performance across the flight envelope is ensured by the use of a multi-model and multi-objective controller design approach. The feedforward function is based on a Doppler LIDAR sensor and the processing of the measurements as well as their physical interpretation combines various ideas from the system identification, the signal processing, and the control design domains. The proposed solution remains very easy to use and tune, thanks to a limited number of parameters that can easily be interpreted physically and that exhibit only very little and very predictable couplings. The performance and behavior of the active load alleviation functions is shown extensively based on a representative flexible long range aircraft model (based on the Airbus XRF1 configuration).

I. Introduction

Inhomogeneous wind fields such as turbulence and gusts are causing variations of the aerodynamic global and local forces and moments that are applied to the aircraft structure. In addition to causing structural loads that the structure should be designed to handle, these additional forces and moments also cause passenger discomfort and anxiety. Active load alleviation of gusts and turbulence is not a new topic: the investigations made on active load control to solve the Lockheed C-5A fatigue issues and leading to the development of the "Active Lift Distribution Control System" (ALDCS) dates back forty years.[1] Already at that time, the trade-off between structure mass and use of active control technologies was present. Historically, within the last forty years, there have been two main drivers for investigations on active load alleviation:

- either a structure design was available, but was for some reasons too weak and the use of active control solved (or was meant to solve) the problem,

- or designers were interested in increasing the efficiency through mass savings thanks to load reductions.

Numerous load alleviation functions have been successfully implemented, for instance on the following airplanes: Lockheed C-5A, Lockheed L-1011-500, Boeing B-1, Northrop Grumman B-2, Airbus A320, Airbus A330/A340, Airbus A380, Boeing 787, Airbus A350. Ref. 2 and the references therein give an interesting overview of the applications of active gust alleviation.

The numerous successes of active control technologies for airplane gust alleviation logically ended up reaching even the maximum technology readiness level (TRL) of 9 for some of these systems. Consequently, the orientation of the research activities of DLR on gust alleviation moved from more classical gust alleviation system design (such as in OLGA[3–5] or LARS[6–8]) to the investigation of more advanced solutions for an even improved alleviation performance. The investigations presented hereafter combine two main ideas:

1. better anticipation capability of future loads for feedforward load alleviation

2. improved controller synthesis methods for multi-objective and robust feedback load alleviation.[9–14]

Previous work had been performed in these directions, especially during the AWIATOR project, and had lead in particular to the GCS[15] and GLAS[16–18] systems and to consider also the use of Doppler LIDAR (LIght Detection And Ranging) sensors for load alleviation purposes (in cooperation with the other project partners).[15–20] As for these previous investigations, the feedforward load alleviation function presented

---
[*]Research Scientist, DLR, Institute of Flight Systems, Lilienthalplatz 7, 38108 Braunschweig, Germany, AIAA Member.
[†]Research Scientist, DLR, Institute of System Dynamics and Control, Münchener Straße 20, 82234 Weßling, Germany, AIAA Member.

American Institute of Aeronautics and Astronautics

hereafter is based on the idea that with a better anticipation of the near future loads a higher load alleviation performance can be achieved. Consequently, in all these systems one of the major components is dedicated to the determination of the expected near future loads. This is realized by gathering information on the wind field ahead of the aircraft, which in the current concept is based on a Doppler LIDAR sensor and a rather extensive processing of the measurements. This information is then used to alleviate (in feedforward) these future loads.

Anticipating the future loads opens new possibilities in terms of load alleviation, but cannot replace a feedback controller that directly acts on the closed-loop behavior of the structural modes. These two parts are radically different and complementary. Therefore the present work also included investigations on load alleviation with a feedback scheme. Flight control law design in general and active load control function (ALC) design in particular are multi-variable control problems where various strict requirements have to be satisfied. In order to cope with uncertainties, missing or erroneous feedback or scheduling variables robustness of the controller is indispensable. To tackle these problems, an optimization-based multi-objective synthesis approach is proposed.[9, 10, 13, 14, 21] Whilst, traditionally, the design of ALC-functions is based on linear flexible aircraft models, see e.g. Refs. 21, 22, the multi-objective optimization-based approach is able to handle nonlinear flexible aircraft models augmented by nonlinear flight control systems.
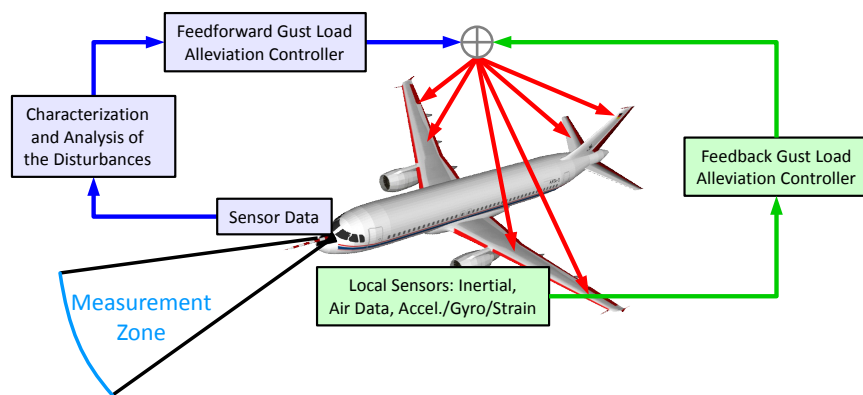
Figure 1. Schematic representation of the feedforward load alleviation principle.

The proposed system architecture consists of a "classical" feedback controller based on the inertial measurements (and if available direct measurements on the structure) and a feedforward controller based on remote wind measurements (see figure 1). Each of both components has capabilities that the other cannot provide (anticipation can only be provided by the feedforward function, whereas modification of the internal dynamics can only be provided by the feedback function). Combining both functions allows a greater load alleviation performance than each function could achieve by itself.

Figure 2 presents the high-level structure of the whole flight control system. The feedback load alleviation function can be seen as an add-on to the regular control laws (later referred to as "EFCS"), which provide the flight control augmentation function (nz-law / C* / C*U / RCAH etc.). These "regular" laws can be developed very early in the design process and are the main drivers for the handling qualities of the aircraft. The other functions (such as feedback and feedforward gust and turbulence load alleviation) are in general trying to satisfy other criteria without deteriorating the handling qualities that are provided by the "regular" laws. The current work focuses only on the feedback and on the feedforward load alleviation functions. Note that in this figure various possible interconnections of the feedforward module with the rest of the system are shown. Not all of these interconnections are always required: the need for each one of them depends on the exact behaviors of the various controllers and thereby on the undesired interactions that might have to be prevented.

Structural loads in an airplane are not only generated by gusts and turbulence but can be caused (among others) by maneuvers or during touchdown and ground operations. In order to optimize weight savings various load cases might need to be considered simultaneously. The focus of this paper is on gust load alleviation and no maneuver load alleviation function is shown hereafter. Note however that a maneuver load alleviation function could easily be added to the active load alleviation functions presented hereafter and the fact that the functions shown hereafter are designed such that they do not deteriorate the maneuverability of the aircraft will be shown.

Section II presents the Doppler LIDAR feedforward control architecture. An explicit wind reconstruction is performed online and is then exploited using a combination of a time-frequency decomposition of the future vertical wind and a decentralized control scheme. This unusual approach permits to easily satisfy the strong and nonlinear control allocation objectives that were specified by the industry partners during the CleanSky Smart Fixed-Wing Aircraft research project. Section III presents the design of the feedback load alleviation function. The control design methodology used is based on the formulation of the design problem as a multi-objective optimization problem. Finally, section IV presents the results obtained on the application to a large and flexible transport airplane benchmark model (derived from the XRF1 model data originally provided by Airbus and integrated in an aeroelastics / flight dynamics model by DLR). The results include the load alleviation performance along the wing and along the horizontal tailplane (HTP) as well as other indicators (e.g. passenger comfort).
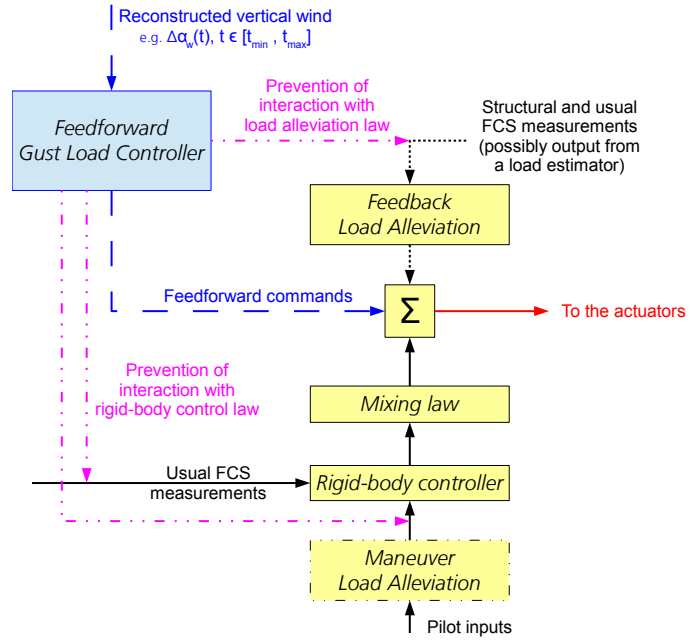

Figure 2. Generic flight control system architecture

II.   LIDAR-Based Feedforward Load Alleviation Controller

In this section, the feedforward load alleviation controller is presented. First, section II.A presents shortly the Doppler LIDAR sensor measurements that are used by the feedforward controller. These measurements are not directly well-suited for use in a feedforward controller and require additional processing steps which are detailed in section II.B. Section II.C presents the "control part" of the feedforward controller and in particular its unusual structure. Finally, the way all these elements were integrated into the simulation environment is presented in section II.D.

II.A.   Remote Wind Sensing with Doppler LIDAR

The basic idea for the gust load alleviation using a Doppler LIDAR sensor is to measure the atmospheric disturbances before they reach the wings of the aircraft and induce additional loads on the aircraft structure. By measuring these disturbances in advance, the load alleviation function can anticipate the future loads and begin counteracting them before having encountered them. This corresponds to the left part of the schematic representation shown in figure 1. The time delay between the measurement and the encounter gust-wings is approximately the distance between the measurement position and the wings divided by the true airspeed. On a typical airliner, the lead time of a measurement at the aircraft nose is small and, as a consequence, the anticipation capability of a feedforward based on these sensors is very restricted. The use of a Doppler LIDAR permits to measure the wind further ahead of the aircraft nose (typically 60-300 m) and thereby to better anticipate the coming gusts and turbulence.

As indicated through its name, a Doppler LIDAR makes use of the well-known Doppler effect, which basically consists in a frequency shift of any observed wave when emitter and receiver (i.e. observer) of the wave are moving with respect to each other. For the sake of simplifying the explanations, only a so-called direct-detection pulsed Doppler LIDAR[19, 20, 23–26] is considered hereafter. Nevertheless, the measurement processing approach and feedforward strategy could easily be adapted to other types/variants of remote wind sensors. In the considered case, a short pulse (typically lasting for a few tens of nanoseconds) of laser light is emitted. The laser beam has a very low divergence, which allows to illuminate only a specific area ahead of the aircraft. The pulse of light advances along in the laser direction and at each location a tiny

fraction of this pulse is scattered by the molecules of the air (and possibly some aerosols if present). The scattering occurs in all / a wide range of directions and part of the scattered light goes back to the the LIDAR sensor. The frequency of the light that is scattered back to the LIDAR sensor can be compared to the one of the light that has been emitted. A shift toward higher frequencies (so-called blue shift) signifies that the sensor and the aerosols/molecules that scattered the light back were moving toward each other. On the contrary, if they are moving away from each other then the wave will be shifted towards lower frequencies (red shift).

If the presence of aerosols can be assumed, so-called coherent heterodyne detection principles with a laser source in the infrared domain are generally the best choice. However, for the alleviation of clear air turbulence at high altitudes (possible lack of sufficient aerosol concentration) and if a high availability of the remote wind measurement is desired, a so-called direct detection principle with a laser source in the ultraviolet domain can be used, since it can work with the so-called Rayleigh-scattering on the molecules of the air. More information on the remote wind measurement technologies and their respective capabilities can be found in the literature, for instance in Refs. 19, 20, 26–30 and references therein.

Ideally the entire wind field ahead of the aircraft would be perfectly known: all three wind components, at every location, and with no measurement error. Due to the fact that the airplane flies at a high velocity and that the bandwidth of the flight control system is limited, a spatial resolution along the flight path higher than 4 to 7 meters is not required. Only the wind information in the close vicinity of the airplane trajectory is required, which with the typical measurement distances (60-300 m) represents only a few degrees in terms of field of view. In terms of wind velocity, the most important component for loads is the vertical component, since this component has the greatest influence on the local lift (via a modification of the angle of attack). The lateral component is only secondary for load alleviation purposes and finally the longitudinal component (i.e. in flight path direction) has an effect on the lift through a change of the airspeed, but this effect remains relatively negligible.

When using Doppler LIDAR sensors, only the relative wind component in the direction of the laser beam is measured. If the wind is measured at locations ahead of the aircraft, then the laser beam (also called line-of-sight) direction is almost collinear with the flight path. With other words, the sensor readings are measuring the least interesting velocity component of the wind (basically the true airspeed) and not the interesting vertical and lateral components.

A way to estimate or reconstruct the missing information (other velocity components as well as the wind at locations that were not directly measured) is to measure the wind at locations with various vertical and lateral offsets with respect to the airplane flight path. The resulting line-of-sight directions are not (all) collinear anymore and the analysis of the differences between the different sensor readings permits to estimate the transversal components (lateral and vertical) of the wind. This method assumes implicitly that the wind is homogeneous between the points where the measurements are made. This assumption is of course difficult to validate and strongly depends on the current atmospheric conditions encountered by the aircraft. The closer the measurements are located, the more likely it is that this assumption is somewhat valid. Reducing the distance (laterally and vertically) between the measurements would however lead to reduce the angles between the different line-of-sight directions, eventually leading to very small differences between the sensor line-of-sight velocities that are measured. This has a major drawback because these measurements cannot be perfect (noise, biases, etc.). In particular, the signal-to-noise ratio (signal being the difference due to the wind transversal components and noise being linked to the noise on each measurement) becomes very poor when calculating the difference between measurements taken under almost collinear directions. With other words, there will necessarily be a trade-off to make between the validity of the homogeneity assumption (linked to the distance of the measurements to the flight path) and the signal-to-noise ratio for the reconstructed transversal wind components.

II.B. Wind Reconstruction

II.B.1. Overview of the Wind Reconstruction Algorithm

In this section, the way a complete wind field was reconstructed from a set of line-of-sight wind measurements is presented. The information on each measurement that will be used for the reconstruction consists of:

- the measurement itself (line-of-sight relative velocity of the sensor with respect to the air at the measurement location)
- and the associated metadata:

- the location in a local reference system at which the measurement was made,
- the orientation of the line-of-sight direction under which the measurement location was observed,
- the inertial speed of the sensor (expressed also in the local reference system) at the time of the measurement.
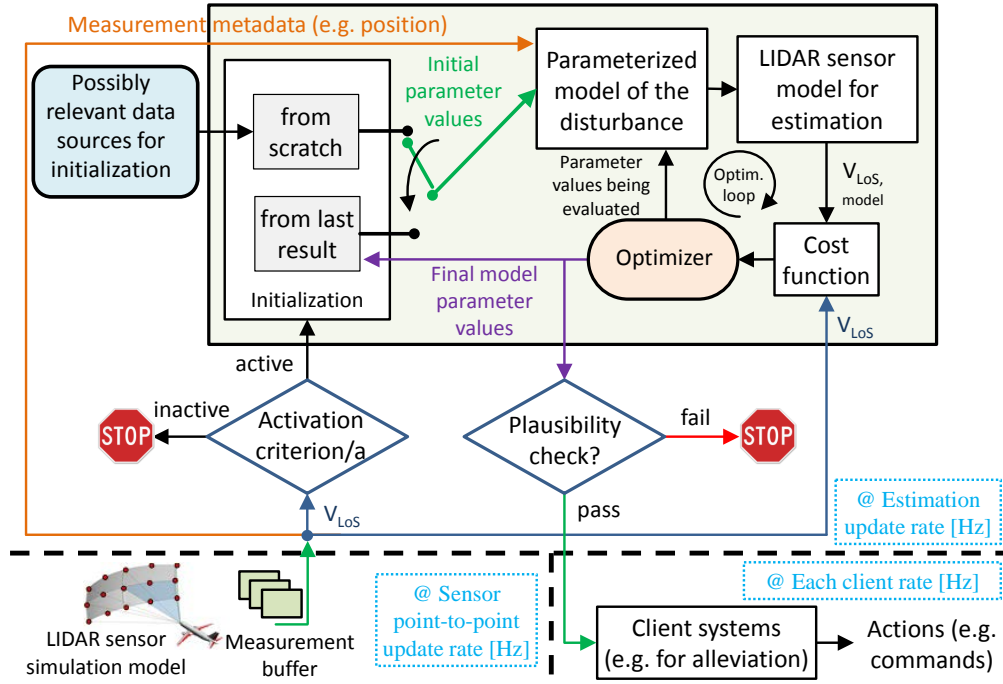

Figure 3. General overview of the wind reconstruction algorithm.

The first step (lower-left part) consists in buffering the measurements (including the corresponding metadata). Depending on the content of the buffer, the main algorithm will be triggered/activated or not. This decision will in general be made based on a very simple computation, such as by defining a deviation index between the measurements and the measurements that would have resulted if the surrounding air would have been perfectly homogeneous. In that particular example, the threshold applied should be set to a higher value than the deviation that will result from the measurement noise.

If the main algorithm is started, it will determine the wind field that explains best the considered measurements. In this process, a parameterized model of the disturbance (gust, turbulence, etc.) will be used and the parameter values be searched. The model used is presented in section II.B.2 and the way the parameter values are searched is presented in section II.B.3.

Finally, once the main part of the wind reconstruction successfully found the "best" parameter values, the plausibility of the obtained wind field is checked prior to any use by the feedforward alleviation functions. It should be noticed that usually at least three different rates are used within the whole system: the buffering rate (synchronous with the sensor rate), the estimation update/wind reconstruction rate (usually relatively low: typically 3 to 10 Hz), and the client system/alleviation function rate (usually the same rate than that of the main flight control computers). This multi-rate decomposition permits to decouple the different steps and to compensate various delays that would otherwise accumulate along the way. The wind reconstruction is performed for a domain, mainly ahead of the aircraft, and is necessarily limited in size due to the fact that the LIDAR sensor itself has a limited range. The time t_d until the aircraft reaches the end of this domain can be approximated by dividing the size of this domain in the direction of the flight path by the current true airspeed of the aircraft. The time t_r between two updates of the wind profile (i.e. execution of the wind reconstruction algorithm) shall ideally be at least two to three times lower than t_d in order to prevent any deterioration of the feedforward performance.

The wind reconstruction process is closely related to the process shown in Ref. 31 for the identification of wake vortices. The strong commonalities as well as the existing differences between these two applications are described in Ref. 32.

American Institute of Aeronautics and Astronautics

II.B.2. Free-Form Wind Field Model

Whereas for other wind reconstruction problems analytical models of the wind field might exist and be applicable for reconstruction problems (see for instance Refs. 31–35 and references therein), gusts and turbulence are stochastic by nature and no particular model structure and shape shall be assumed. Analytical models for gust and turbulence do exist, but are not suited for the considered wind reconstruction. Artificial gust shapes (e.g. $1-$cosine) and artificial turbulence spectrums (Dryden, von Kármán) were defined for certification purposes: they can be considered as "representative" in the sense that they permit to define standardized cases for the computation of structural loads and the certification of the airplane structure. However, they do not represent a wind field shape that can be considered as similar to the real wind fields that will be encountered by the airplane and that was measured with the LIDAR. As a consequence, these models are not adequate for gust/turbulence-related wind field reconstruction.

Very often, when no adequate model can be used to represent the phenomenon of interest (as for the present case), it is still possible to use so-called free-form solutions. Free-form solutions usually carry almost no information on the considered phenomenon in their structure but are often obtained by assuming that the phenomenon of interest can be characterized by a more or less long series of elements. Elements might for instance be pixels for an image or peaks in a spectrum. When dealing with continuous variables or spatial distributions free-form solutions are often based on a possible discretization of the considered variables.

Due to the fact that no alternative solution was found (and seems unlikely to be ever found), a free-form model of the wind field was generated by defining a mesh of the space surrounding the airplane. Each node of the mesh contains the three local wind components at the node's location in the three-dimensional space. The wind vector at other locations (all but the node locations) can be computed by interpolating within the mesh nodes. The main drawback resulting from the use of such a mesh-based free-form model structure is that the number of parameters to estimate can grow very rapidly. Besides, some operations on the mesh have a complexity that have a polynomial dependence on the number of nodes in the mesh. A very fine discretization should consequently be avoided if not absolutely required for the considered problem.

The integrated model used later on only permits to simulate symmetrical (i.e. same disturbance on the left and right wings) gusts/turbulence fields. Consequently the mesh used could be kept very simple without strongly impacting negatively the final results on the cases that can be considered with this model. This mesh is composed only of nodes placed at regular intervals along the flight path of the aircraft. The last point (the furthest ahead of the aircraft) P_n is placed at the predicted location of the aircraft at time "$now + \tau_{lead}$." The first point P_1 is also located along the current flight path but behind the aircraft at the distance $V_{TAS} \ \tau_{lag}$. The exact mathematical formulas that define these two points and all the points in between are:

$$P_1 = P_{ref} - V_{TAS} \ \tau_{lag} \tag{1}$$

$$P_n = P_{ref} + V_{TAS} \ \tau_{lead} \tag{2}$$

$$\forall i \in [\![2, n-1]\!], P_i = P_1 + \frac{i-1}{n-1} \ \overrightarrow{P_1 P_n} \ . \tag{3}$$
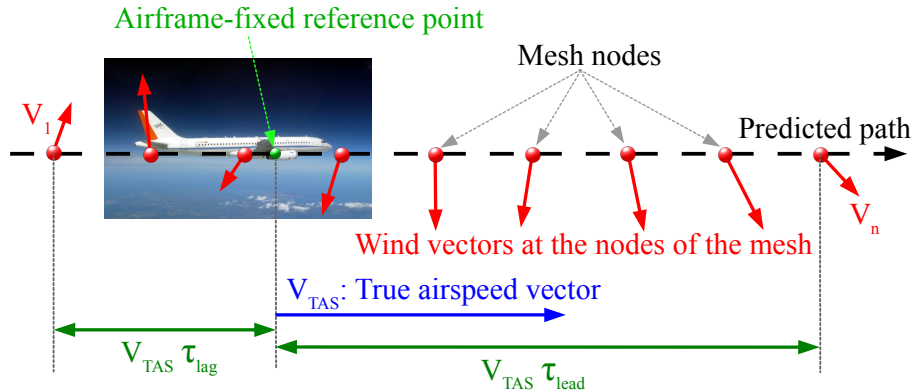

Figure 4. Schematic representation of a 1D-mesh along the current flight path.

Figure 4 shows a graphical representation of this one-dimensional mesh. The local wind vectors associated with the nodes of the mesh are here represented by the red arrows. In the numerical implementation used, these local wind vectors are represented by their components in a North-East-Down reference frame. In this simple 1D-mesh-based model, it is implicitly assumed that the wind vectors at all locations within a plane that is perpendicular to the flight path direction are identical (which means that the wind is constant along any transversal direction). These wind vectors being all equal, they are also equal to the wind vector at the intersection between the flight path and the considered plane. When this intersection is not also defined as a node of the mesh, the wind vector at the intersection is obtained by linearly interpolating between the surrounding two nodes. Typical values permitting to estimate a wind field for load alleviation purposes are:

- Lead-time (τ_{lead}): 1 to 2 seconds
- Lag-time (τ_{lag}): 0.5 seconds
- Number of nodes: ≈ 30.

The values of these parameters have to be chosen based on the characteristics of the system and especially the LIDAR sensor measurement geometry and the aircraft's true airspeed. For instance, placing nodes far beyond the LIDAR sensor range is pointless. However, placing a few nodes behind the current aircraft position is required due to the regularization shown later in Eq. (12). This regularization may create artifacts on the last nodes of the mesh, and consequently it is preferable to let a few nodes behind the aircraft to prevent these artifacts from affecting the reconstructed wind field in the direct vicinity of the current aircraft location. This mesh-based free-form wind field model is the model used in the block called "Parameterized model of the disturbance" in figure 3.

II.B.3.   Maximum-Likelihood Wind Reconstruction and its Regularization

The goal of the wind reconstruction is to interpret the measurements made and make some logical deductions leading to define the most likely wind field that could have caused these measurements. Indeed, only restricted information has been gathered through the measurements and the interpretation/deduction part is crucial and is described hereafter. The process described hereafter corresponds to the "optimization loop" at the top right part of the wind reconstruction process shown in figure 3.

The measurements are usually noted with the letter z and indices are used to distinguish them. Let n be the number of measurements currently contained in the database (or buffer). Then, let

$$\{z_i \mid i \in [\![1, n]\!]\} \tag{4}$$

be the set of measurements used during the wind reconstruction process. Let $\Theta = [\Theta_1, \Theta_2, \ldots, \Theta_p]$ be the vector of all p wind field model parameters. For a given set of parameter values $\tilde{\Theta}$ the n model outputs $\{y_i(\Theta) \mid i \in [\![1, n]\!]\}$ corresponding to the measurements made (same location and conditions) can be computed and compared to the measurements $\{z_i \mid i \in [\![1, n]\!]\}$. The closer the measurements and the corresponding model outputs, the more likely it is that the model used and the parameter values used are right. More formally, for each measurement and each model parameter vector value, a probability density function (pdf) $x \mapsto p(x|\Theta)$ can be used to represent the designer's belief regarding the measurement under the assumption that these model parameters are right.

For the sake of explanation, consider a simple system being a solid with a given mass m whose mass will be measured using a scale and the relationship between mass and weight: $P = mg$. If the gravity field is perfectly known the measured mass is only affected by the sensor uncertainty/error of the scale. The pure sensor error usually has several sources (calibration errors, nonlinearities, quantization, etc.) and can usually be characterized. If the model expressed by the equation $P = mg$ is uncertain (e.g. the equation is approximated or the gravity field itself is uncertain), these model errors and the pure sensor errors combine to form the "measurement error." By describing the stochastic properties of each error source, a model of this measurement error can be derived or estimated. This model describes how likely it is to obtain any particular measurement (here the mass that is deduced from the weight measurement and the model equation) when a given set of system parameters (here the true mass) is assumed. This model can be written as the following pdf:

$$\text{measurement} \mapsto p(\text{ measurement } \mid \text{ system or model parameters }) \tag{5}$$

Taking the notations introduced earlier, the pdf that interests us is the following one:

$$\{z_i \mid i \in [\![1, n]\!]\} \mapsto p(\ \{z_i \mid i \in [\![1, n]\!]\} \mid \Theta\ )\ . \tag{6}$$

In many cases, it can be assumed that the error on each measurement does not depend on the other measurements or that:

$$p(\ \{z_i \mid i \in [\![1, n]\!]\} \mid \Theta\ ) \mapsto \prod_{i=1}^{n} p(\ z_i \mid \Theta\ )\ . \tag{7}$$

Note that this assumption is often satisfied with noise and quantization effects, but usually not when some sensor calibration biases or model uncertainties are present. Coupled sensor errors (e.g. due to calibration or measurement range uncertainties) are not considered in the Gaussian error model used hereafter. It is assumed that proper calibration of the sensor system is made prior to using them or continuously during flight. Precise characterization of the measurement range error or of biases in the standard air data measurements might be less straightforward but at least the synchronization between these two measurement channels can be continuously monitored and corrected.

If the aforementioned assumption is made and when additionally assuming that the pdf of each measurement z_i is (or is assumed to be) Gaussian with mean $y_i(\Theta)$ and standard deviation σ_i:

$$\forall i \in [\![1, n]\!], p(\ z_i \mid \Theta\ ) : z_i \mapsto \frac{1}{\sqrt{2\pi}\sigma_i}\ e^{-\frac{1}{2}\frac{(z_i - y_i(\Theta))^2}{\sigma_i^2}}\ , \tag{8}$$

then the pdf $p(\ \{z_i \mid i \in [\![1, n]\!]\} \mid \Theta\ )$ becomes simply the product of all individual pdfs:

$$\begin{aligned}
p(\ \{z_i \mid i \in [\![1, n]\!]\} \mid \Theta\ ) &= \prod_{i=1}^{n} p(\ z_i \mid \Theta\ ) \\
&= \frac{1}{(\sqrt{2\pi})^n \prod_{i=1}^{n} \sigma_i}\ e^{-\frac{1}{2}\sum_{i=1}^{n}\frac{(z_i - y_i(\Theta))^2}{\sigma_i^2}}\ .
\end{aligned} \tag{9}$$

Note that in these last expressions the Gaussian pdf involves the parameters of the Θ vector only in the expected measurement $y_i(\Theta)$. The uncertainty itself is assumed to result only from the sensor characteristics and not from the strength or the shape of the gust/tubulence field (which are parameterized by Θ). This is a reasonable assumption for the considered sensor technology, but could be invalidated for instance if the sensor uncertainty depends on the measured value (e.g. limited measurement range). Regardless of the exact pdf $p(\ \{z_i \mid i \in [\![1, n]\!]\} \mid \Theta\ )$ that is derived for the problem considered, the maximum likelihood estimation method defines the "most likely parameter vector" $\widehat{\Theta}$ as the parameter combination that maximizes the likelihood to have obtained the measurement set $\{z_i \mid i \in [\![1, n]\!]\}$ that was indeed obtained. This can mathematically be formalized as:

$$\widehat{\Theta} = \underset{\Theta}{\mathrm{argmax}}\ (\ \Theta \mapsto p(\ \{z_i \mid i \in [\![1, n]\!]\} \mid \Theta\ )\ )\ . \tag{10}$$

Note that the notation p and the abbreviation pdf (probability density function) might lead to think of the functions and values mentioned before are "probabilities." In a strictly mathematical sense, they are however not the probabilities or pdf themselves but beliefs on what these probabilities or pdf would be. A detailed explanation as well as the exact differences can be found in the literature on Bayesian estimation (see for instance Refs. 36, 37) and will therefore not be reminded hereafter.

Quite often, instead of maximizing directly the likelihood function $\Theta \mapsto p(\ \{z_i \mid i \in [\![1, n]\!]\} \mid \Theta\ )$, this function is modified in a way that does not modify the location of its maximum. For instance, it can easily be shown (see Refs. 38, 39 for instance for the full derivation) that solving the problem of Eq. (10) is equivalent to solving the least-squares problem of Eq. (11). The fact that the problem of Eq. (11) is a least-squares problem can be exploited by using specialized optimization algorithms (e.g. Gauss-Newton), which can usually converge significantly faster than the non-specialized algorithms (see Ref. 40 and references therein).

American Institute of Aeronautics and Astronautics

On well-conditioned maximum likelihood problems most optimization algorithms should normally find the correct parameter values, the main difference between the algorithms will lie in the computation time.

$$\widehat{\Theta} = \underset{\Theta}{\mathrm{argmin}} \left(\Theta \mapsto \sum_{i=1}^{n} \frac{(z_i - y_i(\Theta))^2}{\sigma_i^2} \right) \tag{11}$$

For the application to the characterization of gust and turbulence using the previously introduced free-form model, it was also found useful to add two Tikhonov regularization terms[41, 42] to the least-squares function, which lead to solve the following regularized optimization problem:

$$\widehat{\Theta} = \underset{\Theta}{\mathrm{argmin}} \left(\Theta \mapsto \sum_{i=1}^{n} \frac{(z_i - y_i(\Theta))^2}{\sigma_i^2} + \alpha_1 \, ||\Gamma_1 \, \Theta||^2 + \alpha_2 \, ||\Gamma_2 \, \Theta||^2 \right). \tag{12}$$

The used Tikhonov regularization matrices Γ_1 and Γ_2 are respectively of sizes $(p-1) \times p$ and $(p-2) \times p$ (with p being the number of parameters in the vector Θ) and respectively penalize the first and second derivatives of the reconstructed wind profile. To this end Γ_1 is based on the coefficients $[-1, +1]$ and Γ_2 is based on the coefficients $[-1, +2, -1]$ of the well-known Mexican Hat wavelet/convolution filter (also called Laplacian-of-Gaussian filter)[43] of order two.

$$\Gamma_1 = \begin{bmatrix} -1 & +1 & 0 & \cdots & \cdots & \cdots & 0 \\ 0 & -1 & +1 & \ddots & \ddots & \ddots & \vdots \\ \vdots & \ddots & -1 & +1 & \ddots & \ddots & \vdots \\ \vdots & \ddots & \ddots & \ddots & \ddots & \ddots & \vdots \\ \vdots & \ddots & \ddots & \ddots & -1 & +1 & 0 \\ 0 & \cdots & \cdots & \cdots & 0 & -1 & +1 \end{bmatrix}, \quad \Gamma_2 = \begin{bmatrix} -1 & +2 & -1 & 0 & \cdots & \cdots & \cdots & 0 \\ 0 & -1 & +2 & -1 & \ddots & \ddots & \ddots & \vdots \\ \vdots & \ddots & -1 & +2 & -1 & \ddots & \ddots & \vdots \\ \vdots & \ddots & \ddots & \ddots & \ddots & \ddots & \ddots & \vdots \\ \vdots & \ddots & \ddots & \ddots & -1 & +2 & -1 & 0 \\ 0 & \cdots & \cdots & \cdots & 0 & -1 & +2 & -1 \end{bmatrix} \tag{13}$$

This choice permits to penalize wind fields containing small-scale variations: the small-scale variations are expected to not be well measured by the LIDAR sensor and not be the components of the wind field for which it is beneficial to anticipate and to begin counteracting them very early anyway. The coefficients α_1 and α_2 permit to tune the relative strength between the Tikhonov penalization and the least-squares criterion. It was found that even small values of these coefficients (i.e., not massively changing the overall shape of the profile found on the tested cases) were already well penalizing nonsmooth profiles and also helping some of the optimization algorithms to converge more quickly.

II.B.4. Results of the Wind Reconstruction Process

The behavior of the wind reconstruction is illustrated in figure 5 for a standard $1-$cosine gust. The true vertical wind along the flight path is shown in black and the successive wind reconstruction results are shown in cyan. The wind reconstruction algorithm was called every 0.3 seconds during the simulation. The parameters of the free-form mesh-based model (see section II.B.2) were set to the following values: $\tau_{lead} = 1.6\,\mathrm{s}$, $\tau_{lag} = 0.5\,\mathrm{s}$, and $N = 33$. A centered Gaussian noise with a standard deviation of $1.5\,\mathrm{m/s}$ was added to the line-of-sight measurements. Note that each result is a wind profile, which is symbolized by a curve. Due to the fact that the successive reconstructed wind profiles overlap partly and are very similar, the different cyan curves can hardly be distinguished in this representation. The overlapping of the successive results shows that the wind reconstruction is behaving in a very consistent manner. The strong similarities of the wind profiles (even in the local estimation error) cannot be caused by a reuse of information between the successive runs of the algorithm because each run is initialized with a zero wind at every location and no information whatsoever is saved between the runs. The strong similarities between the results are the consequence of the fact that many of the measurements considered during two successive runs of the wind reconstruction algorithm are the same. Indeed, the measurement buffer (see lower-left part of figure 3) is significantly larger than the number of new measurements that were made between these two runs. More detailed results can be found in Ref. 44.

It can be noticed in figure 5 that the reconstructed gust does not reach the maximum value of 15 meters per second that was here set for the gust. This is a consequence of the regularization term that was introduced

to improve the smoothness of the reconstructed wind profiles and to prevent the reconstruction problem from being ill-posed. The difference in terms of gust amplitude is here negligible compared to the benefits that this regularization brings. The wind profiles in figure 5 can be seen as the sum of a general trend and some additional smaller amplitude oscillations. The former is the interesting part of the signal that the feedforward controller will have to act upon, whereas the latter is not really correlated to the disturbance but rather to the measurement noise and shall not be alleviated. A filtering approach that is capable of selecting the former and of rejecting the latter is included as the first step of the feedforward control strategy shown hereafter in section II.C.

The computational cost for the wind reconstruction problems that were solved during the simulation shown in figure 5 was always lower than the chosen sampling time (0.3 seconds). The algorithm was implemented with only very simple operations (additions, multiplications, very few divisions that can be protected) and does not rely on matrix inversions, computation of eigenvalues or singular value decompositions. This performance was obtained with an implementation that focused on flexibility and not on speed. As a consequence, a significant reduction of the computational cost shall be achievable with a quite moderate effort.
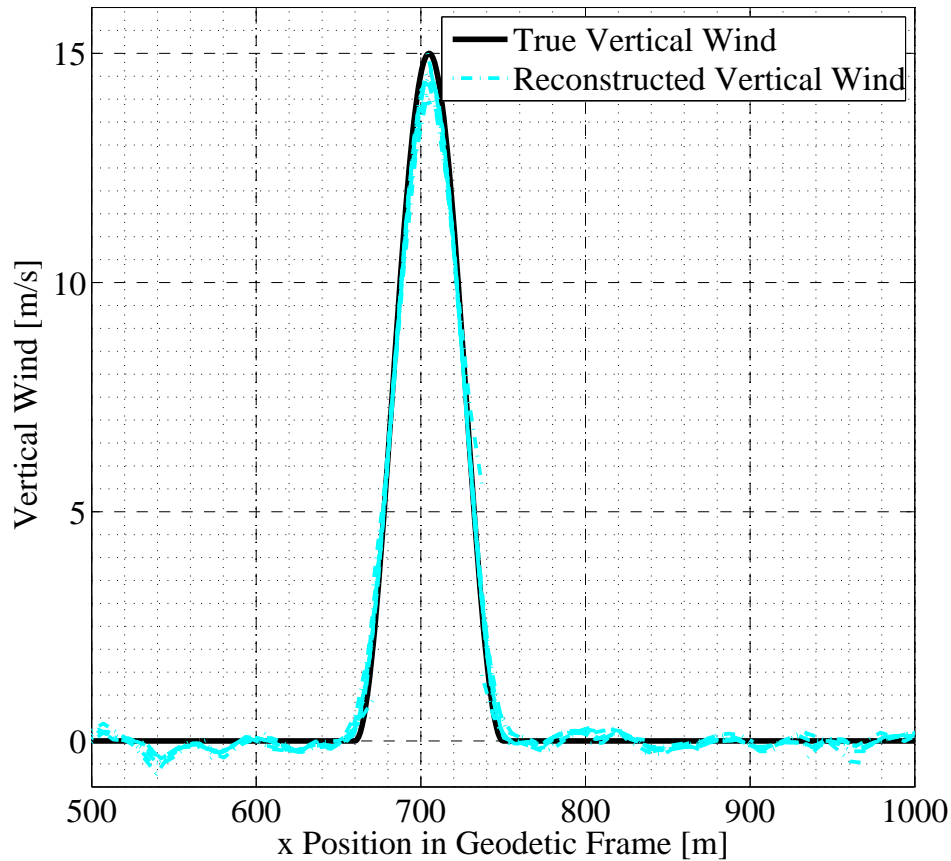

Figure 5. Comparison between the real vertical wind and the reconstructed vertical wind for the example of a standard 1−cosine gust. Reconstructed wind from different runs included.

II.C.   Feedforward Load Alleviation Controller

II.C.1.   Basic Idea

In the specification of the desired load alleviation behavior made by the load specialists, a typical wording came repeatedly: "small-amplitude disturbances should not be alleviated using the spoilers." While this sounds and definitely is reasonable from an airplane performance point of view, this implicitly specifies

American Institute of Aeronautics and Astronautics

that a highly nonlinear allocation constraint is desired for the controller. This constraint makes the direct[a] application of some of the most powerful tools and results in control theory impossible. It also raised the question of defining a simple controller structure, which can easily be tuned and permits to obtain such a highly nonlinear behavior. Pitching the aircraft up or down is the most effective way to change the aerodynamic loads. For an effective load alleviation based on pitching actions and with a restricted bandwidth, the pitching commands shall be initiated before encountering the disturbance. After having considered the motivations for such a desired alleviation behavior, the practical aspects regarding structural loads at the HTP and the fuselage as well as for passenger comfort, the proposed alleviation concept was finally expressed as follows:

- The low frequencies of the atmospheric disturbances should be alleviated by pitching the airplane up or down. For passenger comfort reasons, it shall be possible to select a different behavior for small-amplitude disturbances or even to restrict this behavior to large-amplitude disturbances (i.e. relevant for peak loads).

- In the medium-frequency range:

  - The tuning parameters should allow to choose whether disturbances with very small amplitudes in the medium-frequency range are alleviated or not (e.g. to avoid unnecessary actuator cycles, or to reduce power consumption).
  - The disturbances with relatively small amplitudes should be alleviated using only trailing edge deflections or camber variations (i.e. basically with ailerons but possibly also with innovative flaps if available).
  - The larger disturbances should be alleviated with any possible means, including spoilers or any other suitable control device even if they tend to deteriorate the airplane's aerodynamic performance.

- The higher-frequency components of the disturbance will not be alleviated at all with the feedforward function.

The limits between "low," "medium," and "higher" frequencies as well as the thresholds between "very small," "small," and "larger" amplitudes are tuning parameters for the feedforward load alleviation function. Note that the bandwidth of the feedback load alleviation function (section III) might be tuned to be higher than the one of the feedforward function. There is a priori no reason to impose any relationship between the bandwidths of the feedforward and feedback gust alleviation functions. However, the achievable wind sensor spatial resolutions will probably limit the effective bandwidth of the feedforward gust alleviation function.

II.C.2. *Implementation Using the Fast Orthogonal Wavelet Transform*

The design of the gust and turbulence load alleviation concept that was just described is clearly not straightforward. It must behave strongly nonlinearly in some frequency ranges and consist of at least two completely separated types of alleviation: one based on local actions on the wing and the other based on pitching the aircraft up or down. At the same time the phase lag of the alleviation commands should not be too high, otherwise the effectiveness of the load alleviation will vanish. Since a piece of the future wind profile is known in advance, it is actually possible to perform the required filtering operations without adding phase lag.

The concept proposed here is very unusual but relies on a very simple idea: the filtering and highly non-linear allocation between the different alleviation substrategies will be enforced by a preprocessing step. Note that even if the developed controller structure has been fully driven by the requirements of the considered application, the resulting concept and structure can certainly be useful for numerous other applications.

The overall architecture resulting from the direct application of the aforementioned idea to the feedforward load alleviation controller can be represented schematically by the block diagram of figure 6. A time-frequency transformation/decomposition of the signal that is known partly in advance (here the wind ahead of the aircraft) is performed first. The exact result of this operation depends on the time-frequency technique used, but the information contained in the original signal is now expressed as "at this point in time, the signal contains these frequencies with these amplitudes and phases" whereas it was previously expressed as "at

---

[a]Note that indirectly, after having exploited the structure proposed hereafter to decompose the control design problems into several subproblems, the advanced tools provided by linear control theory can actually be applied to each of the resulting control design subproblems.

this point in time, the signal had this value." With most techniques, no information is lost and the inverse transformation can be defined. The capacity of restoring the original signal is indeed very important for the proposed architecture and the inverse transformation is required in a later step.
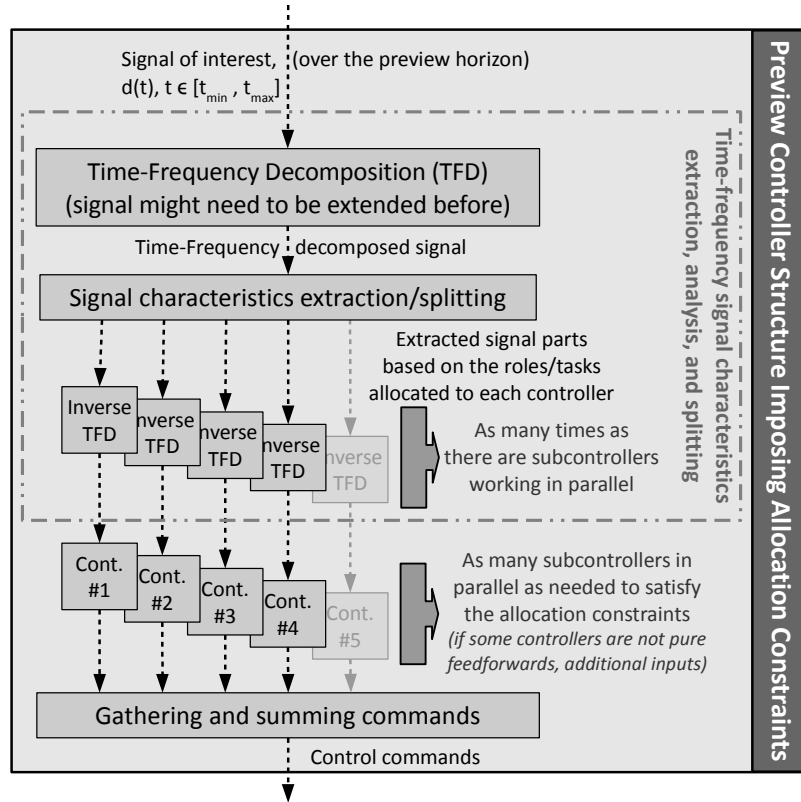
Figure 6. Overall structure of the feedforward load alleviation with allocation constraints.

The following step is to select the components of the signal that are of interest for the system and to process them. For the sake of example, the high-frequency noise of a signal could be removed by erasing the corresponding transformed data (e.g. the amplitude coefficients for all frequencies higher than a given threshold can be set to 0). If the altered transformed representation of the signal would be transformed back into the time domain, it would seem that the original signal was low-pass filtered but with no phase shift. The nonlinear behavior desired for the pitching actions (i.e. only consider low-frequency high-amplitude components of the signal) can be obtained by selecting only the low frequencies of the signal and among them neglecting the components whose amplitudes are below a certain threshold. By transforming the remaining components back into the time domain, it would appear that the desired characteristics have been separated from the rest of the signal. The transformations performed are detailed in a few lines after the end of this short overview.

Once back in the time domain, the various signals that are obtained by using this preprocessing can then be used by several controllers working in parallel, which can each have a very restricted and well defined role, which can be realized very easily. For instance, the low-frequency high-amplitude part of the signal can be given as input to a simple controller that can only provide an additional elevator command: the tuning of such a function is very simple as is the validation of its behavior. Another controller can take care of some medium-frequency parts of the signal and only be able to provide symmetrical aileron commands.

The concrete implementation that was made uses the so-called Fast Orthogonal Wavelet Transform (FOWT), which is a so-called time-scale technique and not a time-frequency one, but the basic idea remains the same. This implementation is detailed in the next section. The proposed feedforward structure (figure 6) can be used with most time-frequency/scale techniques and similar results should be achievable. Here, the FOWT technique was chosen, because it is simple to implement, requires little computing resources, and the obtained time-scale decompositions are easy to interpret and to work with.

The development of wavelet transforms was a major step in local time-frequency decomposition of continuous and discrete signals.[45, 46] The complete theory of the various wavelet transforms and their use for signal processing goes far beyond the scope of this paper. Consequently, only a few remarks required to understand the approach used for the signal characteristics extraction and signal splitting used in the proposed feedforward controller will be provided here. For a deeper insight into wavelet theory and applications the reader is referred to Refs. 45, 46. The Fast Orthogonal Wavelet Transform (FOWT) is one particular type of wavelet transform. It allows to decompose a discrete time signal in several successive steps. Each step leads to a decomposition of the signal into

- its approximation or general trend (lower-frequency part)
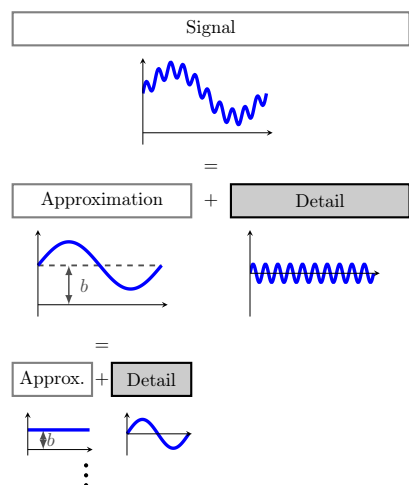- its details (higher-frequency part).

The obtained approximation is undersampled (factor 2) at the end of each decomposition step. This undersampling is performed by keeping only the elements with an odd index. This operation shrinks the length of the remaining signal and can be seen as a multiplication of the sampling time by a factor two. The fact that the vector of filter/wavelet coefficients is not modified while the sampling time is doubled causes a reduction of the frequency band of the wavelet (the cutting frequencies are divided by two). By repeating this process several times, several frequency bands are successively extracted. This general process is schematically represented in figure 7. The decomposition preserves time-wise correlation, which means, that information about the signal characteristics at a certain time is still available. Furthermore, each signal can be recomposed with an inverse process using the obtained approximations and details.

These decomposition steps are based on convolutions of the signal, i.e. the original signal at the first step or the approximation of the signal at the current step with a pair of complementary discrete filters. In the discrete wavelet terminology, a decomposition step leads to increase the level/scale by one and later the reconstruction steps will correspond to a decrease of the level/scale. The original signal is usually considered to be level 0. The complementary property leads to have (at each level) the sum of the signals corresponding to the "detail" and the "approximation" part equal to the original signal.

For the type of processing that is considered in this paper, it is very important to use a wavelet basis for which perfect reconstruction filters with a finite impulse response exist. This allow to reconstruct easily the original signal from its decompositions (with other words this allows to define the inverse transform). The filters used for reconstructing the signal (i.e. for restoring the signal based on its decomposition in a series of coefficients) are different from the filters used for decomposing it. This leads to have four filters, noted D_h, D_l, R_h, and R_l hereafter: D and R respectively stand for decomposition and reconstruction and the indices h and l stand for high-frequency (i.e. detail part) and low-frequency (i.e. approximation part).

Figure 7. Schematical representation of the signal decomposition steps based on the FOWT (from Ref. 47)

Note that not all wavelet bases permit to define a perfect inverse transformation (i.e. the original signal can be recovered with no loss/error). The so-called bior3.9 wavelet, which was chosen in this work, permits a perfect reconstruction. Its numerical values can be found in the literature (e.g. in Refs. 45, 48).

Figure 8 presents a generic block diagram for a signal manipulation in the time-scale domain. The decomposition filters D_h and D_l are applied in combination with undersampling operations to decompose the input signal (a_0) in several steps. In this figure, the decomposition was made up to the third level. However, the number of decomposition levels should be chosen for each application and relates to the lowest frequency band to be decomposed. The fact that the input signal has a limited length limits the number of decomposition levels that can be used (each undersampling operation shortens the signal) and therefore the lowest frequency band that can be considered. In the considered application to feedforward active load alleviation, this property was limiting the anticipation capability. As a consequence the signal (noted a_0 in figure 8) had to be artificially extended before applying the FOWT. Indeed, the area ahead of the aircraft for which the wind information can be reconstructed based on the LIDAR measurements is limited in size due to the limited sensor range. Increasing the measurement range (if possible) is expected to cause a significant

American Institute of Aeronautics and Astronautics

deterioration of the measurement quality (higher noise levels). This limited domain size is an issue for the extraction of the low-frequency content of the wind profile, which is meant to be alleviated with pitching commands. The proposed solution consists in extending the wind field artificially: for this, a long-term wind average is taken as "best guess" for the wind at locations far from the reconstructed profile and an exponential function is defined for the transition between each extremity of the wind profile and this averaged wind. The wind is determined using the inertial and air data measurements (the LIDAR sensor can be part of the air data measurements) and a relatively long-term average of this wind can easily be computed (e.g. by a simple low-pass filter). Making this artificial extension converge to the observed average instead of zero is meant to increase the robustness of the solution against slight sensor calibration errors and also against relatively large areas with non-negligible mean vertical wind (e.g. thermal effects, turbulence, lee waves, or downbursts). The time-constant τ_{decay} for the exponential decay shall be set to a value in the neighborhood of the inverse of the lowest frequency $f_{GLA,low}$ that is worth to consider for the load alleviation functions (i.e. $\tau_{decay} \in [\, 0.2/f_{GLA,low} \, , \, 5/f_{GLA,low} \,]$). Note that this artificial extension is only used (and good!) for the lowest frequency band.

On the right of the block diagram shown in figure 8, the reconstruction operations based on the filters (R_h and R_l) and on the insertion of zeros between the samples (counterpart of the undersampling operations in the decomposition).
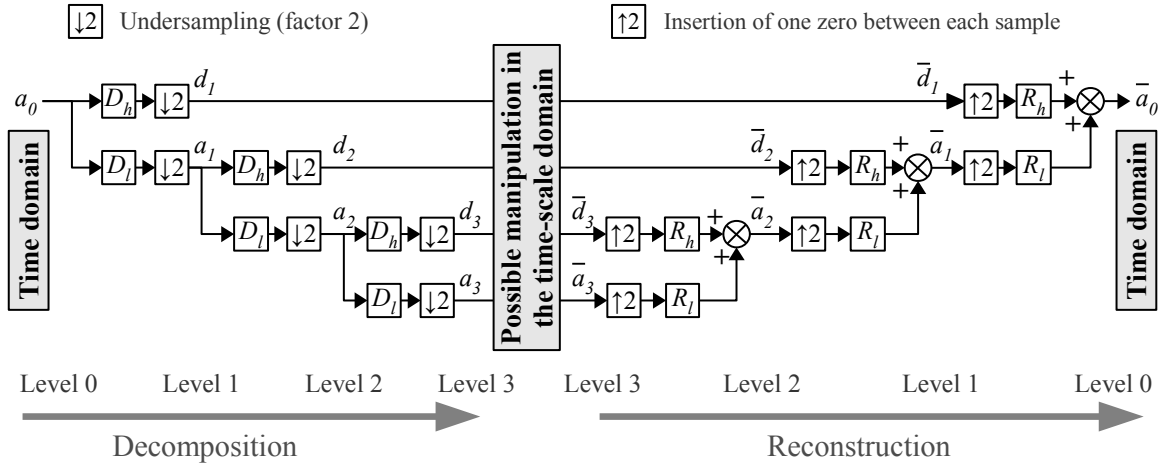
Figure 8. Representation of the signal decomposition and reconstruction based on a filter bank implementation of the FOWT. The decomposition is shown up to level 3. The blocks D_h, D_l, R_h, and R_l are convolutions with the corresponding filters. In the middle of this figure, the location at which a module for analysis and manipulation of the signal in the time-scale domain can be inserted is represented.

In the middle of figure 8 the place at which a manipulation of the signal in the time-scale domain can be performed is indicated. The technique used to manipulate the coefficients at a given level such that low-amplitude coefficients are ignored is commonly known as "wavelet thresholding" or "wavelet shrinkage." The two most common thresholding functions are the so-called soft and hard thresholding functions. The soft thresholding can be interpreted as a dead-zone: the coefficients smaller (in absolute value) than the chosen threshold are set to zero whereas the threshold magnitude is subtracted from the others. This leads to effectively ignore the low-amplitude parts of the signal but also reduces the amplitude of the larger ones and thereby possibly prevents to reach the maximum achievable alleviation performance. The hard thresholding behaves as a threshold: values lower than the threshold are suppressed (set to 0), whereas values greater than the threshold are not modified. This leads to a discontinuity at the threshold which can cause artifacts in the reconstructed signals at times for which the successive wavelet coefficients are spread on both sides of the threshold.

The desired shrinkage function shall be zero (or very small) for small input values, converge to the linear function $y = f(x) = x$ for x large, and be continuous and tunable in between (but not necessarily smooth). The "smooth sigmoid-based shrinkage" family of functions (SSBS)[49–51] satisfies all these requirements and also provides a few additional degrees of freedom. It reads:

$$\delta_{t,\tau,\lambda} : \mathbb{R} \to \mathbb{R}, \ x \mapsto \frac{sign(x) \ max(0, |x| - t)}{1 + e^{-\tau(|x| - \lambda)}} \quad . \tag{14}$$

The role of the parameters t and λ can easily be understood based on figure 9. The parameter τ defines the abruptness of the transition between the point $(0, t)$ and the asymptotes $y = f(x) = x - t$ in $+\infty$ and $y = f(x) = x + t$ in $-\infty$. In the application considered in this paper the additional degree of freedom provided by t is not used and the value of t is always set to 0 here. This corresponds to a case where the SSBS function behaves as a soft threshold for amplitudes far below the threshold λ, behaves as a hard threshold for amplitudes far above the threshold λ, and provides a smooth transition between these two behaviors in the neighborhood of the threshold λ.

Wavelet thresholding based on the aforementioned SSBS functions is used to separate the wind profile signal characteristics that are interesting for load alleviation and whose induced loads are alleviated with different strategies: "pitching actions," "aileron commands only," and "aileron and spoiler commands." The specification of the limit between the low-frequency range (that will be alleviated by means of pitching commands) and the medium-frequency range (alleviated with the actuators on the wing) can easily be made by defining that this limit shall occur between decomposition level (i.e.

Figure 9. Representation of the SSBS function (blue line). Asymptotes at $+\infty$ and at $-\infty$ are respectively represented in red and in magenta. The black dashed line represents the $y = x$ function.

number of decomposition stages in figure 8) P and level $P - 1$. The signal to be used for the pitching actions is then based on the selected decomposition level P, assuming during the reconstruction process that all detail coefficients at the lower levels (i.e. $P - 1$, $P - 2$, ..., 0) were equal to zero. Similarly, the signal containing the remaining frequencies (all but the low frequencies) can be reconstructed by using the coefficients at levels $P - 1$ and below and by ignoring the coefficients from level P.

This strategy permits to split the signal into several frequency bands but still does not restrict the pitching-based alleviation to large amplitude disturbances: for this the coefficients at level P are modified using the wavelet thresholding technique based on SSBS functions with $t = 0$. In order to completely filter out the higher frequencies a level R (with $R < P$) can be defined and the "detail" coefficients for the levels between 0 and R can simply be set to zero.

The signal extracted by the operations described above is the signal that is later passed to the first or "pitching commands" controller, which can be seen as the block labeled "Cont. #1" in figure 6. The second and third controllers ("Cont. #2" and "Cont. #3") can act on the wing control surfaces: only on the ailerons in the case of controller 2 and both on ailerons and spoilers in the case of controller 3. Both are working in the same frequency band but controller 2 is the only one active for small disturbances and controller 3 becomes active for larger disturbances.

A similar signal extraction via wavelet thresholding with an SSBS function as for controller 1 is first applied to the intermediate levels (levels $P - 1$ and below). Then for each of the considered levels the obtained wavelet coefficients are distributed to either controller 2 (the small ones) or controller 3 (the large ones). Indeed, the distribution is performed in a smooth manner using a logistic function $l_{B,M}$ for each of the considered levels.

$$l_{B,M} : \mathbb{R} \to [0, 1], x \mapsto \frac{1}{1 + e^{-B(|x| - M)}} \tag{15}$$

The function $l_{B,M}$ defines a coefficient between 0 and 1 such that for small x the value is (very close to) 0 and for large x it is (very close to) 1. So for a given wavelet coefficient c_{23} that was selected to be alleviated either by controller 2 or by controller 3, the coefficients c_2 and c_3 that correspond to the respective parts to be alleviated by controller 2 and by controller 3 are defined as follows:

$$c_2 = (1 - l_{B,M}(c_{23}))\ c_{23} \quad \text{and} \quad c_3 = l_{B,M}(c_{23})\ c_{23} \tag{16}$$

Note that regardless of the definition of the function $l_{B,M}$, the following relationship holds: $c_{23} = c_2 + c_3$. Consequently, the $l_{B,M}$ function defines the distribution of c_{23} onto c_2 and c_3. From the definition of $l_{B,M}$ the role of both parameters can easily be understood:
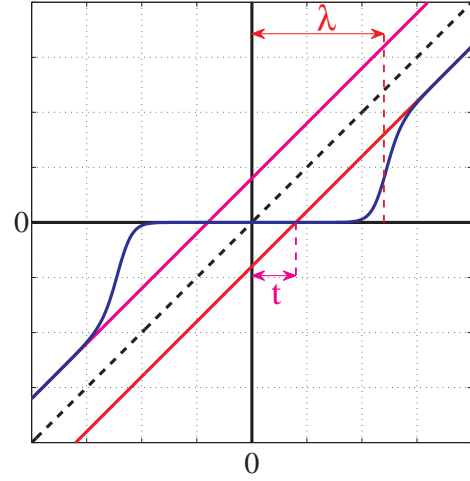
American Institute of Aeronautics and Astronautics

- M defines the location (here a threshold on the wavelet coefficient amplitude) whereat the transition between controllers 2 and 3 is occurring: when the coefficient is equal to M then 50% of it is taken care of by controller 2 and the other 50% by controller 3.

- B defines the growth rate: a large value for B causes an abrupt transition between 0 and 1.

The desired behavior necessarily corresponds to cases for which $B > 0$ and $M \geq 0$. The smoothness of this distribution is desirable in order to ensure that slight changes in the estimated wind profiles (leading to a slight increase/decrease of c_{23}) cannot result in a "jump" in the distribution of c_{23}, i.e. a drastic variation of c_2 in one direction with an almost equally large variation of c_3 in the other direction.

II.D.   Simulink Implementation

The wind reconstruction algorithm described in section II.B and the feedforward load alleviation function with time-frequency allocation constraints described in section II.C were integrated into the flight dynamics/aeroelastics Simulink model of the aircraft considered (see the application shown in section IV). Most of the operations performed for the wind reconstruction and in the feedforward controller are significantly easier to implement with an imperative programming language than with a graphical language. Consequently, they were programmed in C++ and included as Simulink s-functions in the model. Figure 10 shows the overall structure of this implementation. The block diagram of figure 10 contains two s-functions and a subsystem between them. The first s-function contains the real wind field (required for the proper simulation of the flight physics, see blue inputs and outputs) as well as the LIDAR sensor simulation and the wind reconstruction algorithm (sections II.A and II.B). The second s-function contains all the elements described in section II.C. Both s-functions and the artificial signal extension could have easily been integrated into a single s-function: this decomposition was made with the aim of possibly allowing future project partners (who might not have access to the source code) to reuse the wind reconstruction algorithm with another feedforward controller by just replacing the second s-function block.
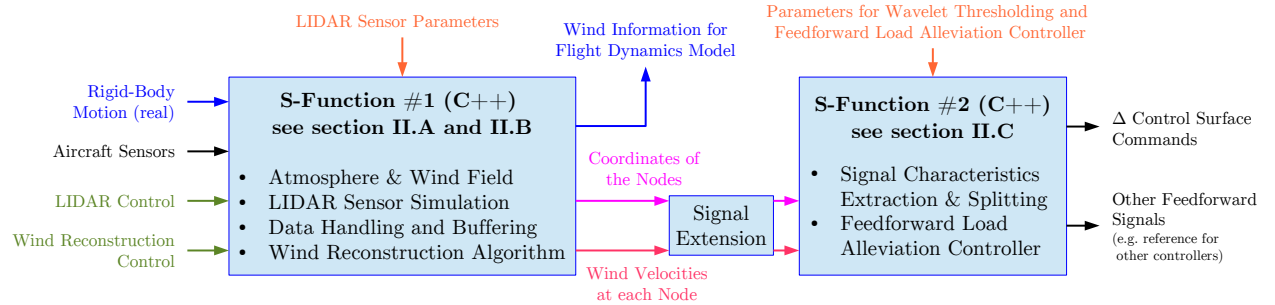
Figure 10. Structure of the GLAREWISE+TFAC load alleviation function implementation in Simulink.

Both s-functions have also inputs allowing the configuration of the elements they simulate and also to foresee a dynamic change of parameters at simulation/run time. These inputs are shown in orange at the top of figure 3. The first s-function also needs the aircraft sensor readings (including sensor dynamics, errors, etc.) for some of the computations as well as some control signals to determine the LIDAR sensor scanning motion, when and where new measurements are performed, and when the wind reconstruction shall be executed. Note that the LIDAR sensor simulation here is a parameterized and high-level sensor simulation, which takes the wind field and a series of generic parameters as inputs and produces "representative" (blurring effect, measurement uncertainties, etc.) measured velocities in the line-of-sight (laser beam) direction. This is therefore an extremely simplified high-level model of a very complex system for use in an integrated environment. In Ref. 24 and references therein the way a direct detection Doppler LIDAR sensor, including the interferometer system, can be modeled more precisely can be found. This type of modeling is necessary but not suited for rapid and integrated (several disciplines) simulation programs: this situation is quite comparable to the use in such simulations of simplified aerodynamic models instead of RANS-CFD computations.

The feedforward controller (second s-function) can act on all control surfaces by adding deflections compared to the ones computed by the regular flight control laws (called EFCS later on) and to the ones of the feedback controller presented in the next section. Additionally, other commands (second output port of the

second s-function) can be used to act directly on other places of the control loop, such as for instance by generating an additional load factor command for the EFCS and FBALC (presented in section III) functions. The pitching actions were originally planned to be realized by means of an additional load factor command, but the tests showed that directly commanding an elevator deflection was more reactive and improved significantly the alleviation performance. The best way to command these pitching actions is still unclear and shall be investigated further: the implementation made is well suited to perform these investigations.

III.   Optimization-Based Multi-Objective Robust Control Law Synthesis

III.A.   Overview of the Optimization-Based Multi-Objective Robust Control Law Synthesis Methodology

Flight control law design is a multi-variable control problem where various strict requirements have to be satisfied. In case of uncertainties, missing or erroneous feedback or scheduling variables robustness of the controller is indispensable. To tackle these problems, an optimization-based multi-objective synthesis approach is proposed.[9, 10, 13, 14] The main features of this methodology are:

1. that various kinds of design objectives can be taken into account in their most natural form (e.g. initial response, overshoot, loads, comfort),

2. that design alternatives can be assessed most visibly with respect to given requirements,

3. that robustness can be considered in various ways (e.g. multi-model approach, robustness criteria).

In case of various, usually conflicting, design objectives the designers need to be able to compare different designs and they need to know up to which extent a design objective is achieved. In case of conflicts they need quantitative information about degradation in individual objectives while other objectives are improved. Such performance indices or criteria should accurately reflect the design objectives and provide a comprehensive measure of the achieved design quality. Mathematical formulation of design objectives as criteria also allows the computer to distinguish different designs. Multi-objective optimization, as a computer-aided design technique, is able to take care of all the various conflicting design goals individually, but compromising them concurrently. In case of available quantitative information about requirements and demands the problem can be solved by transforming the set of criteria into a weighted min-max optimization problem, where the weights are chosen according to the demands. On the other hand to explore system performance in the criteria space no quantitative information about requirements and demands is necessary. In that case the problem must be solved as a vector optimization problem leading to a Pareto-optimal solution set.

The whole process of robust control law synthesis based on multi-objective optimization is performed in several steps. At each step of this process, one or more optimization problems are solved numerically. The results of these optimizations are analyzed by the designer. In multi-objective optimization there usually exists no unique "optimal" solution, but a (usually infinite) set of Pareto-optimal solutions, called compromise solutions, for which an improvement in one design objective may cause degradation in one or more of the other objectives. The designer tries to find the best overall compromise given the various, usually conflicting objectives and constraints. As long as the designer is not fully satisfied with the current solution, new options (e.g. change of controller structure) might be considered and lead to start a new design step. In order to ease the use of numerical optimization techniques, quantitative and normalized representations of the various objectives are required (see section III.A.3). This normalization of the objectives and constraints is also very helpful for the detection of possible deficiencies over the range of parameter uncertainty. Model uncertainties should always be considered in model-based design, as no model can be assumed to be perfect. Note that optimization techniques can also be used to find "worst-case" parameter combinations to decide whether a design is robust or not.

III.A.1.   Controller Structure and Parameterization

Compared to many other control design techniques, directly optimizing the controller parameters – as it is done in the proposed multi-objective design method – permits to avoid restrictions in terms of structure and properties (e.g. linearity) for controller and model. The controller structure can be chosen in a problem-adequate way taking advantage of the designer's knowledge and prior expertise. In classical controller structures the parameters to be tuned are the gains and filter constants. In (linear) control theory there

exist several analytic controller synthesis methods, which guarantee structural stability properties. Such methods are for example LQR-synthesis, eigenstructure assignment or μ-synthesis. In any synthesis method there are some free parameters to be determined by the designer in order to define the controller completely. Since the controller structure is arbitrary in multi-objective design, it is possible to incorporate synthesis formulae (like μ-synthesis) into the computational procedure. Hence structural properties of the controller are guaranteed by the synthesis formulae while the synthesis parameters are properly tuned according to the design criteria by multi-objective optimization.

III.A.2. System Model Description and Robustness

In principle, there is no particular restriction on the model structure, the types of disturbance to consider, or the simulation tool (linear, nonlinear, multi-body simulation software, etc.), as long as they permit to evaluate/simulate the entire system for the design cases and to recover the corresponding results. Robustness of the controller to be designed can be achieved in several ways by appropriate mapping of the robustness requirements onto the design criteria.

1. "Local" robustness criteria

   Robustness of the controller "around" a design point can be enforced in the multi-objective approach by adding suited robustness criteria (e.g. gain/phase margins) to the set of performance criteria.

2. "Global" robustness using the multi-model approach

   Robustness against structured parameter deviations is achieved by applying a common controller to a set of fixed "worst-case parameter" system models. This model set characterizes the range of dynamics variations within the range of operation. For each of these models the appropriate list of criteria has to be specified. By combining all criteria together, the problem to design a common controller for several system models simultaneously is transformed to a so-called multi-model multi-criteria design problem. In general there exists no theory that guarantees stability or performance robustness across the range of operation, if only a finite number of operating points is considered. If deficiencies exist in some points, the according operating point has to be added to the multi-model set and a re-design has to be done.

3. Robustness via risk computation using Monte Carlo simulation

   Fast simulation code gives the possibility to use Monte Carlo-based risk computation within the synthesis loop. In a Monte Carlo simulation not only a few "worst-case parameter" system models are considered simultaneously, but a lot of simulations are performed with randomly disturbed parameters. However, the performance criteria are not treated separately for each model but are combined to statistical characteristics like mean, standard deviation or risk probabilities which serve as robustness objectives. This means that the requirements stated in JAR-AWO 131 or FAR 25 as well as many others can be used as synthesis criteria directly.

III.A.3. Criteria Formulation

In engineering design there exist a lot of characteristic quantities to judge design results. But these quantities do not necessarily have the required property of a mathematical criterion needed for multi-objective design. Without loss of generality we can assume that an optimization criterion has to be positive real and is to be minimized. Any arbitrarily defined scalar characteristic quantity ν can be transformed into a compliant criterion form c by the following transformation:
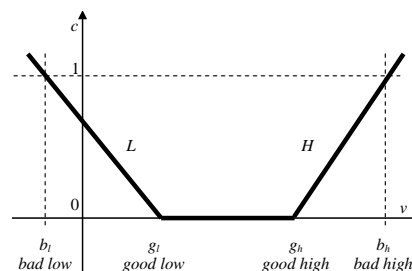
Figure 11. Transformation of characteristic quantities to optimization criteria.

$$
\begin{aligned}
c &= max(L(\nu), 0, H(\nu)) \\
L(\nu) &= (\nu - g_l)/(b_l - g_l) \quad , \text{with } b_l < g_l \\
H(\nu) &= (\nu - g_h)/(b_h - g_h) \quad , \text{with } g_l < g_h < b_h
\end{aligned}
\tag{17}
$$

Each characteristic quantity ν must be transformed like this individually if necessary. The transformation described in Eq. (17) and illustrated in figure 11 maps any quantity to a non-negative real number and the

transformation parameters b_l, g_l, g_h, b_h have to be chosen according to the following fuzzy-like description of the objective goal in terms of "bad" and "good":

- A characteristic quantity ν is considered to be satisfactory or good for values between g_l and g_h.

- It is considered as not acceptable or bad for values less than b_l or greater than b_h.

By such a transformation satisfactory characteristic quantities are mapped to zero (or almost zero due to the approximation of the max-function). This means that a satisfactory characteristic quantity makes no contribution to the overall objective function. However, if a characteristic quantity becomes unsatisfactory, the criterion value increases and contributes to the overall objective again and may be traded-off between other objectives if a conflict arises.

III.A.4. *Assessment and Wort-Case Search for Increased Robustness*

Any designed control law has to be assessed whether the requirements are satisfied over the whole flight envelope for any possible combination of uncertain parameters. The problem is how to detect deficiencies. Assume that the uncertain and operational parameters are bounded and combined in a vector P. Of course, any criterion or constraint $c_i(P,T)$ is also a function of P. Deficiency detection can now be formulated as a global optimization problem

$$\max_P \max_i \left(c_i(P,T)/d_i \right) \quad , \text{subject to} \quad c_j(P,T) \leq d_j \tag{18}$$

with the same criteria or constraints as defined for design.[12] A deficiency occurs if the optimization results in a value greater than one. In order to be sure to detect the overall maximum, global optimization procedures are necessary with large computational costs. However, experience showed that in the case of insufficiently robust solutions, 'local' optimization procedures are usually able to find local bad/deficient solutions very rapidly and which are sufficient for the next design step. The robustness can be improved by adding the bad cases found in the considered multi-model set and by restarting the optimization on this augmented problem. When dealing with parameter-varying systems, the analysis of the bad cases can also help to detect possibly missing scheduling parameters for the controller.

III.B. Design of a Feedback Control Alleviation System for the Benchmark Model

III.B.1. *The Benchmark Model*

The design of the feedback active load controller (FBALC) is based on the project's benchmark model described in Ref. 52. From the delivered flight cases it was possible to consider a cruise flight scenario with a speed of about 175 m/s described by the data of the two flight cases Ma = 0.86 at Height = 8279 m and Ma = 0.5 at Height = 0 m.

The FBALC to be developed should be robust against load variations. These variations are covered in the benchmark model by the 7 load cases F000, FA2M, FA2T, FA9M, FA9T, FC8T and FT8T. Gust disturbances are modeled as discrete 1−cosine gusts with different gust lengths of 30, 150, 300 and 350 ft. Only vertical gusts are considered.

III.B.2. *Feedback Control Law Structure*

The principle structure of the FBALC is a simple feedback of the IRS-sensed vertical acceleration signal `az_sens` on symmetric ailerons, spoilers and elevators. Only longitudinal motion is considered. Each surface has its own loop consisting of gain, saturation limits and a low-pass filter to suppress high-frequency excitations. Thresholds (noted $l_{\text{elevators}}$ l_{ailerons}, and l_{spoilers} hereafter) are introduced to avoid activity of the FBALC already for small accelerations. Inner and outer ailerons and the elevator use the same threshold. The threshold for the spoiler feedback signal is higher than the other. Hence spoilers are activated only for heavy gusts. Vertical acceleration pilot commands are filtered with a third-order linear filter scheduled by Mach number and mass:

$$\forall i \in [\![0,3]\!], \ C_i = C_{i,0} + (Mach - Mach_{ref}) \, C_{i,Mach} + (mass - mass_{ref}) \, C_{i,mass} \tag{19}$$

$$\dot{x} = \begin{bmatrix} 0 & 1 & 0 \\ 0 & 0 & 1 \\ -C_1 & -C_2 & -C_3 \end{bmatrix} x + \begin{bmatrix} 0 \\ 0 \\ 1 \end{bmatrix} \delta_{pitch,normalized} \qquad (20)$$

$$\Delta a_{z,cmd} = \begin{bmatrix} C_0 & 0 & 0 \end{bmatrix} x \qquad (21)$$

The commanded vertical acceleration is compared to the measured acceleration and used in combination with a threshold function T, a proportional controller K_i, and a cut-off filter $F(s)$, as shown in Eqs. (22-24).

$$n_{z,error} = (a_{z,cmd} - a_{z,sensor})/g \qquad (22)$$

$$\forall i \in \{\text{elevators, ailerons, spoilers}\}, \quad \delta_i = F(s) \ K_i \ T(n_{z,error}, l_i) \qquad (23)$$

$$\forall (x,y) \in \mathbb{R} \times \mathbb{R}^+, \text{ if } |x| >= |y|, T(x,y) = x, \text{ otherwise } T(x,y) = 0 \qquad (24)$$

III.B.3.   Design Goals and Applied Loads and Comfort Criteria

The overall design goals for the FBALC are:

- Robust gust load alleviation at wing root.
- Compliance with design loads at all other load stations under consideration.

  Since design load values are not available in this benchmark the design goal will be to keep an increase of loads at other stations than the wing root as small as possible.

- Do not degrade passenger comfort, improve if possible.
- No effect on handling qualities.

The loads criteria considered are the RMS/Max/Range-value of shear force F_z, bending moment M_x and torsion M_y as response to a $1-$cosine gust at the stations modeled for the benchmark aircraft.

Passenger comfort is measured as a global comfort criterion for seated persons according to the ISO 2631-1 standard.[53] It is a frequency-weighted criterion based on IRS vertical acceleration $a_{z,sensor}$.

The effect of the FBALC system on handling qualities and maneuverability is not explicitly considered during the design.

III.B.4.   Design Setup

The design is performed applying the optimization-based multi-objective robust control law synthesis approach described in section III.A. Robustness of the control law is incorporated by the multi-case approach outlined in section III.A.2. The design scenario under consideration and the available data allow for 56 different cases covering flight conditions, mass, and gust variations. These cases are combinations of the 7 load cases available, the two Mach/altitude combinations as well as the four different gust lengths. To reduce the computational burden 8 cases have been selected representing the most critical cases regarding the design goals. These cases are the combinations of load case FA2T with Mach 0.5 and Mach 0.86 and the four gust lengths of 30, 150, 300 and 350 ft.

For each cut station the RMS, maximum and range values of the shear force F_z, the bending moment M_x and the torsion moment M_y are computed. Only the right cut stations are considered since the flight scenario is symmetric. For each case this results in 276 loads criteria which have to be taken into account during optimization. The six criteria concerning the loads at the wing root have to be minimized, the remaining 270 loads criteria are treated as constraints with prescribed upper bounds reflecting the limit loads for each station.

The proposed control law structure has seven parameters to be tuned: four gains of the feedback loops for inner/outer aileron, elevator and spoilers; two threshold parameters and one cut-off frequency of the identical low-pass filters to avoid high-frequency excitations.

American Institute of Aeronautics and Astronautics

IV. Results for the XRF1-Based Benchmark Model

IV.A. Performance of the Feedback Active Load Controller (FBALC)

IV.A.1. Load Alleviation

Several multi-objective optimization runs have been performed to achieve the following results. The runs have mostly been necessary because of the lack of information about the design loads. Hence several evaluations of proper upper bounds for the constraints representing the design loads have to be done.

The quantitative result is (partly) depicted in figure 12. It shows the achieved criteria values in parallel coordinates for four cases representing different gust lengths. The color of the ordinate axes (green, red, blue) indicates the usage of the criterion for minimization, as constraint or for observation only (passive). The criteria values are connected by a line. The red line shows the values for a gust response without FBALC whereas the blue line is with FBALC. It can be seen that loads can be reduced at many stations for almost all gust lengths considered (blue below red). Only for the shortest gust with a length of 30 ft almost no improvement could be obtained, which is not problematic since the loads are small in this case.
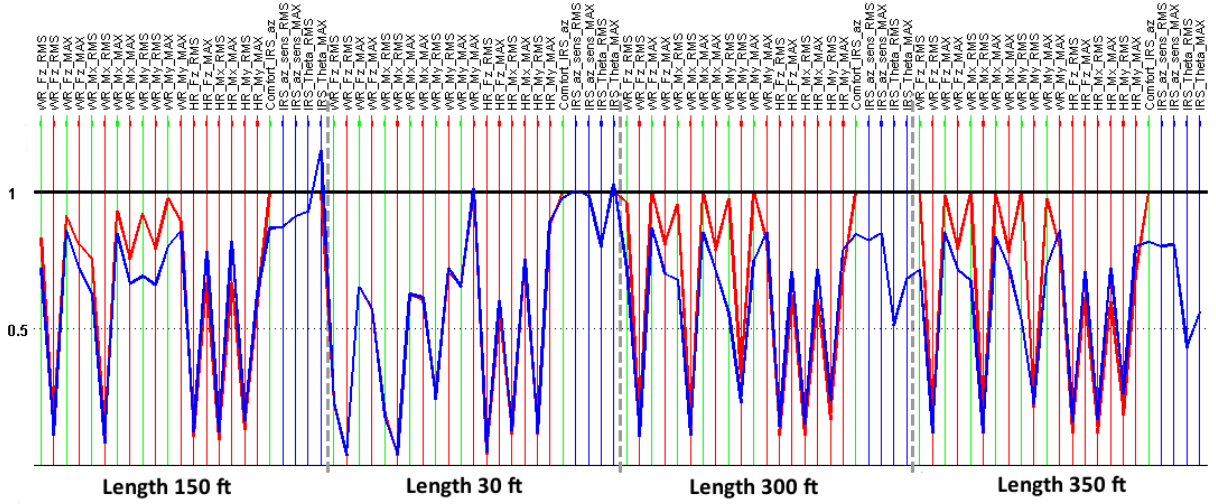

Figure 12. Criteria representation in parallel coordinates, cases with different gust lengths (red: FBALC off, blue: FBALC on).

To get more physical insight loads are considered along the wing and the horizontal tailplane (HTP). 35 stations were defined along the each wing, and 11 stations were defined along each side of the HTP. For each of these stations and for each of the 56 available cases (flight point, mass, gust, etc.) the loads time series (as result of a simulation in the time domain) were evaluated based on three metrics: RMS, range (max−min), and maximum/peak value. Each of the 168 results ($56 * 3 = 168$) obtained for each station can be analyzed separately but global performance indexes are also very useful to avoid being overwhelmed by the amount of performance indexes. The average and maximum loads in the 56 cases are considered and combined with the three metrics (RMS, Range, max). This leads to six performance indexes per load station and per loads type. The three considered loads types are the shear force (F_z), the bending moment (M_x), and the torsion moment (M_y). One of the most critical location in order to enable weight savings is the wing root. The 18 performances indexes (6 indexes and 3 loads types) for the wing root are shown in table 1. The multiplicity of the indexes is linked to the fact that they physically relate to various interesting quantities. For instance, the mean of all cases in terms of the RMS and of the range will be rather interesting for fatigue, whereas the maximum peak values in all cases will rather be interesting for the required overall strength of the structure.

All the aforementioned criteria were taken into account for all wing and HTP stations during the present work. For conciseness reasons, only the maximum (over all 56 cases) of the RMS and peak loads are shown in figures 13 and 14. These figures show that the shear force (F_z) and bending moment (M_x) loads are reduced both in RMS and peak value along very large portions of the wing (left side plots). Only torsion M_y is slightly increased at some of the stations 3 to 35 of the wing. A consequence of the active load alleviation controller is that the maximum RMS values of shear force F_z and bending moment M_x are increased for the

HTP (two top right plots in figure 13). These increased values are however still below the prescribed level for design and were consequently accepted. All other measures (including those not shown here) indicate an overall decrease of HTP loads.

Table 1. Load reductions at wing root obtained with the FBALC

	Mean			Maximum		
	RMS	Range	Max/Peak	RMS	Range	Max/Peak
Shear force F_z	10%	10%	6%	12%	1%	1%
Bending moment M_x	17%	15%	6%	17%	12%	9%
Torsion moment M_y	26%	22%	9%	20%	20%	10%
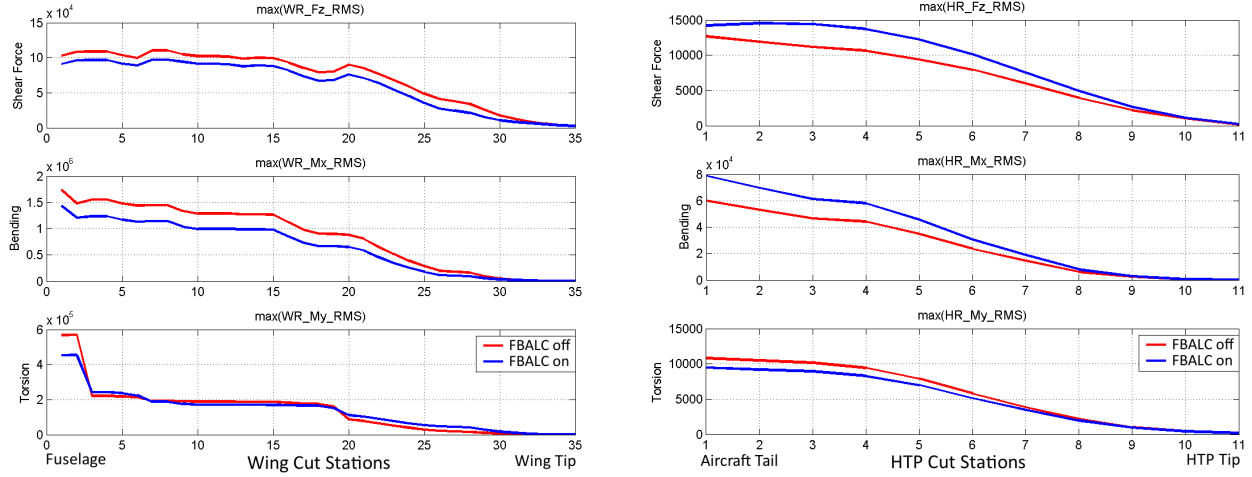
Figure 13. Maximum RMS values of loads F_z, M_x, and M_y along the right wing (left side plots, 35 cut stations) and the right HTP (right side plots, 11 cut stations).
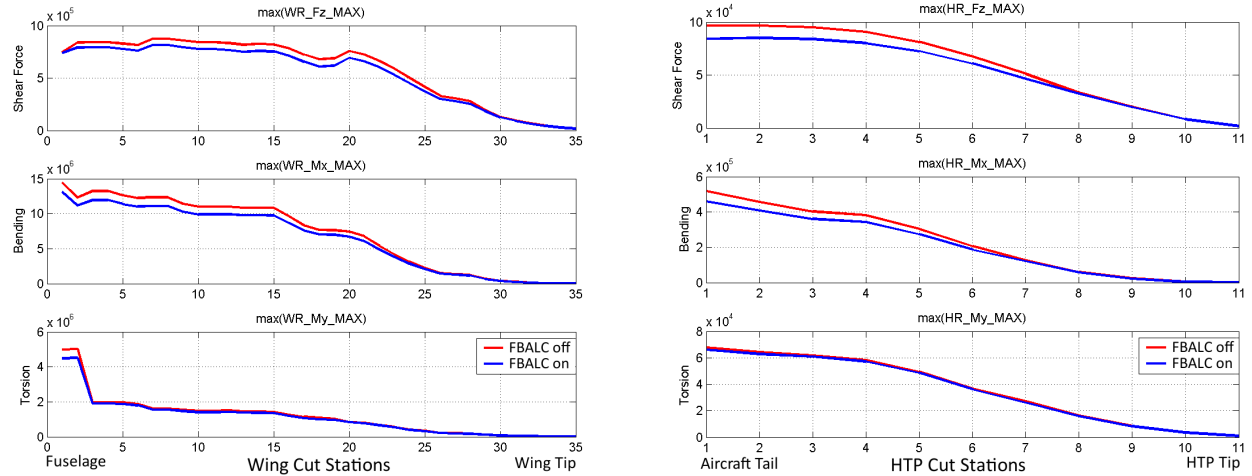
Figure 14. Maximum peak values of loads F_z, M_x, and M_y along the right wing (left side plots, 35 cut stations) and the right HTP (right side plots, 11 cut stations).

American Institute of Aeronautics and Astronautics

IV.A.2. Behavior During Pitch Maneuvers

The effect of the pre-filter to compensate pilot input and thereby decoupling active loads control from maneuver-induced vertical accelerations is demonstrated in figure 15. A 1 g maneuver was simulated for load case FA9M at Mach 0.5. The gust applied had a length of 150 ft and, when present, started at $t = 2.5\,s$. From figure 15 it can be seen that – as desired – vertical acceleration as well as the control surface deflections are not affected by the FBALC controller during the maneuver in the absence of gust: the green line (no gust, FBALC on) lies exactly on the black line (no gust, no FBALC). However, when a gust was applied the FBALC controller reduces accelerations also during the maneuver. The lower three diagrams of figure 15 show the control effort necessary for gust load alleviation. The additional elevator deflection is quite small, whereas the symmetrical deflections of the ailerons and of the spoilers are up to 5°. Though not shown here (results can be found in Ref. 44) the gust loads at the wings and HTP are reduced by the designed FBALC controller when active and in the presence of the gust (compared to the case without active load alleviation and in the presence of the gust).
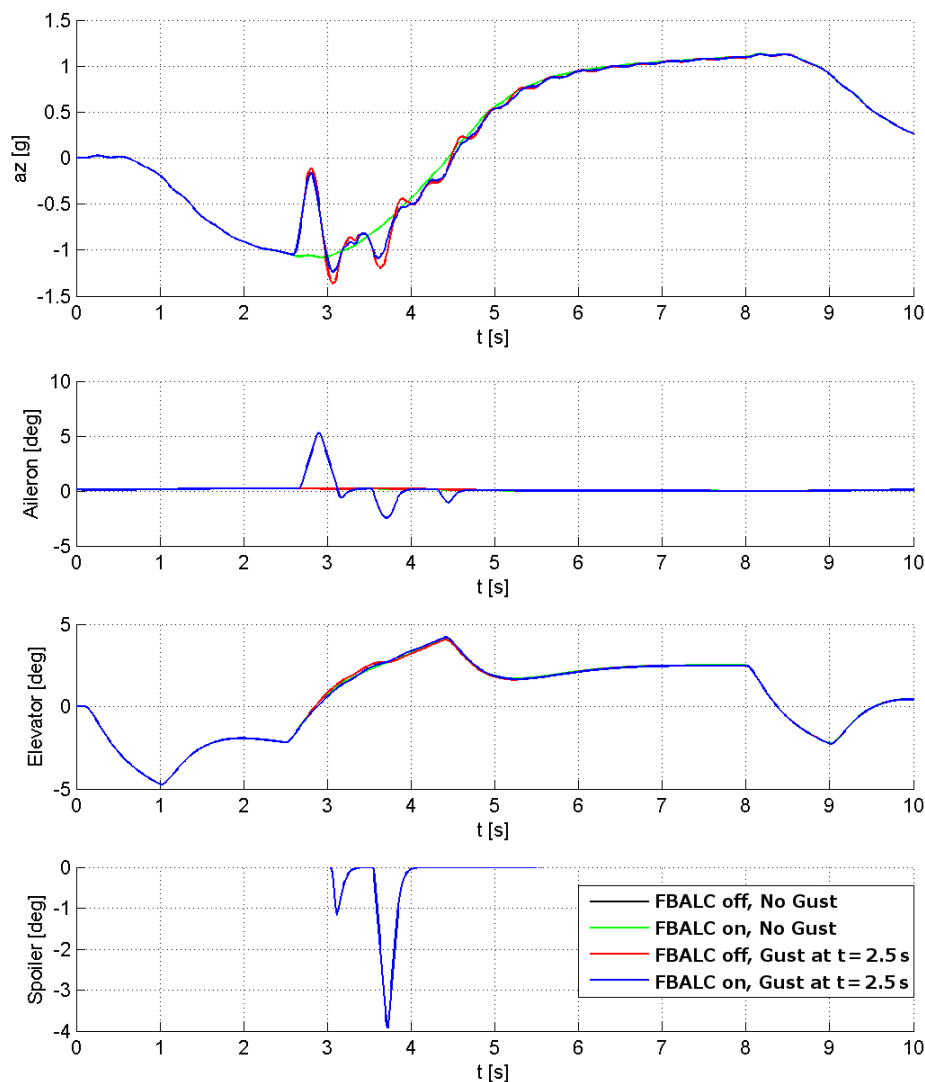

Figure 15. Response of the vertical acceleration a_z and control surfaces during a 1 g maneuver: with/without gust and with/without active load alleviation. (Mach 0.5, load case FA9M, gust length 150 ft).

American Institute of Aeronautics and Astronautics

IV.A.3. Impact on Comfort

The structural modes of large flexible aircraft tend to be of lower frequencies (than those of small and more rigid aircraft) and to negatively impact the passenger comfort. In Ref. 53 comfort criteria based on the ISO 2631-1 standard[54] are defined. They comprise "low frequency comfort" determined by vibrations but also motion sickness phenomena caused by very low frequencies. Those criteria are very well suited for the multi-objective integrated design of flight control laws and gust load alleviation functions.

In this application comfort improvement was not of primary interest. The goal was to not decrease comfort while gust loads are alleviated. The comfort criterion was therefore used as a constraint with upper bounds corresponding to the values of the FCS-augmented aircraft: the basic controller serves as baseline and the FBALC is not allowed to deteriorate the comfort values compared to this baseline. In figure 16 three bar charts are depicted showing the comfort indexes achieved for a 1−cosine gust of length 30 ft, 150 ft and 350 ft respectively. The 14 cases correspond to the possible combinations of Mach number (2) and load cases (7). It can be seen that comfort is positively affected by the FBALC system for longer gusts. For short gusts the comfort index remains unchanged and does not exceed the design demands as required.
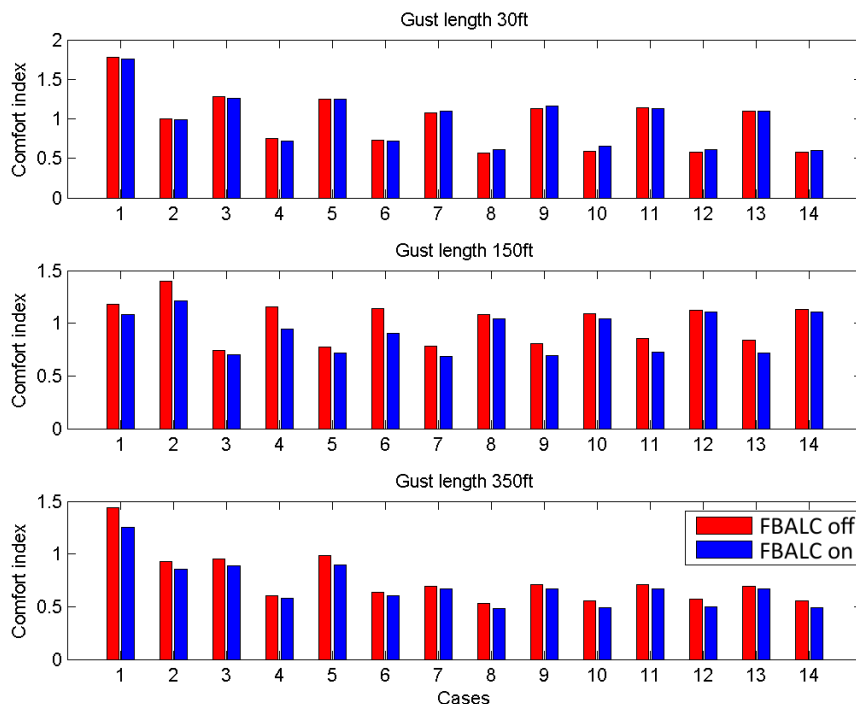

Figure 16. Comfort index for 3 different gust lengths and the 14 possible combinations of Mach and load cases.

IV.B.   Performance of the Integrated Feedback and Feedforward Load Alleviation Functions

A simulation model that couples both the feedback load alleviation function (FBALC) that was presented in section III and the feedforward load alleviation function ("Gust Load Alleviation using REmote WInd SEnsors and Time-Frequency-based Allocation Constraints" or GLAREWISE+TFAC) that was presented in section II was developed. It was used to make a first evaluation of the load alleviation performance improvement achieved by the feedforward load alleviation (GLAREWISE+TFAC) in comparison to the load alleviation performance of the feedback load alleviation (FBALC) alone.

Three cases will be exemplarily shown hereafter for various gust encounters:

1. Only basis flight control system or EFCS (typical Airbus-like n_z-law in the pitch axis and rate-command/attitude-hold in the roll axis)

2. EFCS and FBALC

3. EFCS, FBALC, and GLAREWISE+TFAC.

The GLAREWISE+TFAC function is not meant to be used without feedback load alleviation. The combination EFCS and GLAREWISE+TFAC is therefore not considered hereafter. The considered gusts have a one-minus-cosine (1−cosine) shape and all have the same amplitude here. Their lengths are: 30 ft, 150 ft, 300 ft, and 350 ft. They were considered in both directions: upward and downward.

Figure 17 shows the results of the simulations for the 350 ft and 300 ft gust lengths and figure 18 shows the results of the simulations for the 150 ft and 30 ft gust lengths. On both figures and for each simulation the wing root bending moment is shown on the left and the vertical load factor n_z in the middle of the cabin on the right. The black line corresponds to the "EFCS" case, the dashed magenta line corresponds to the "EFCS and FBALC" case, and finally the dash-dotted cyan line corresponds to the "EFCS, FBALC, and GLAREWISE+TFAC" case. The anticipation capability of the GLAREWISE+TFAC function can easily be seen by the fact that the dash-dotted cyan line begins to vary before the other two: this variation is mainly due to the pitching command that anticipates that loads in the opposite direction are expected to occur very shortly after. In all these simulations the gusts begin at the time t = 6 seconds. The first seconds are not shown here and are not relevant for the load analysis: during this time the aircraft flies simply in its trimmed condition. These seconds need however to be simulated in order to bring the internal states (e.g. LIDAR measurement database) of the GLAREWISE+TFAC function to a representative state for the various algorithms that are being tested (number of measurements in the buffer, spatial distributions of these measurements, etc.). Note that depending on the sensor and wind reconstruction algorithm configurations, six seconds might be more than really necessary for this initialization.

For the 150 ft gust cases (both directions), the FBALC function improves significantly the wing root bending moment and the GLAREWISE+TFAC function only minimally improves it further. For the larger gust lengths (300 ft and 350 ft), the load reduction achieved by the FBALC function is also significant, but this time the GLAREWISE+TFAC function achieves a significant additional load reduction. For the 30 ft gusts, the load reductions are very moderate for both "EFCS and FBALC" and "EFCS, FBALC, and GLAREWISE+TFAC" cases. The first peak is even slightly larger when the load alleviation functions are active. Note however, that the reached load levels in the 30 ft cases are very far from the critical loads.

The GLAREWISE+TFAC function also significantly reduces the range of variation of the load factor n_z, as can be seen on the right side of figures 17-18. The prevention of relatively long-lasting negative load factors (see downward gusts of lengths 300 ft and 350 ft) or their significant reduction (see downward gust of length 150 ft) are likely to be found beneficial by most passengers. The applicability of the commonly used comfort criteria[53, 54] to this type of cases is however questionable and therefore these metrics were not used to quantify the comfort on these particular cases. Further investigations aiming at quantifying the impact of the GLAREWISE+TFAC function on comfort should be performed.

Even though both functions (FBALC and GLAREWISE+TFAC) were developed separately and not retuned together yet, they can be combined and provide significant improvements for the longer gust scales. The alleviation performance of the combined feedback/feedforward gust load alleviation function shows promising results already. A significant amount of work shall however still be spent improving both parts and making them work better together. In the presently shown coupling the feedforward function does not really "inform" the feedback function of its actions, which therefore leads the feedback function to consider some of the anticipated actions made by the feedforward controller as "disturbances that should be alleviated". How much additional load alleviation improvement (i.e. on the top of the improvement shown here) could be obtained thanks to a better cooperation between both functions is not known and certainly very difficult to estimate. Generally speaking, the evaluation of the performance and the behavior of functions such as the GLAREWISE+TFAC can hardly be done without a complete and fully coupled (atmosphere, aeroelasticity and loads, LIDAR sensor, nonlinear equations of motion, etc.) simulation environment as the one used in this work.
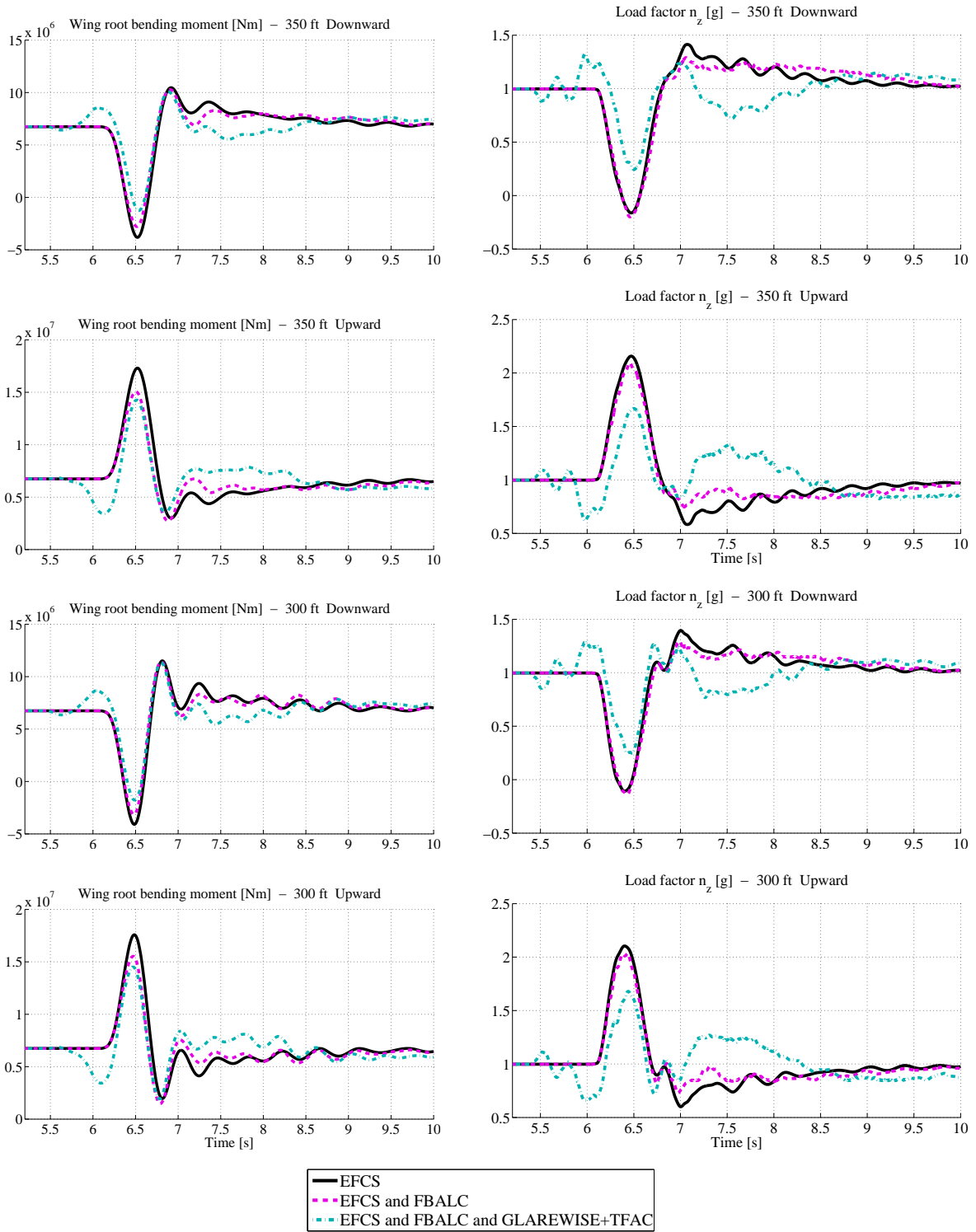
American Institute of Aeronautics and Astronautics

Figure 17. Comparison of wing root bending moments (left) and vertical acceleration at middle of cabin (right) over time during encounters with 1−cosine gusts of length 350 and 300 ft.
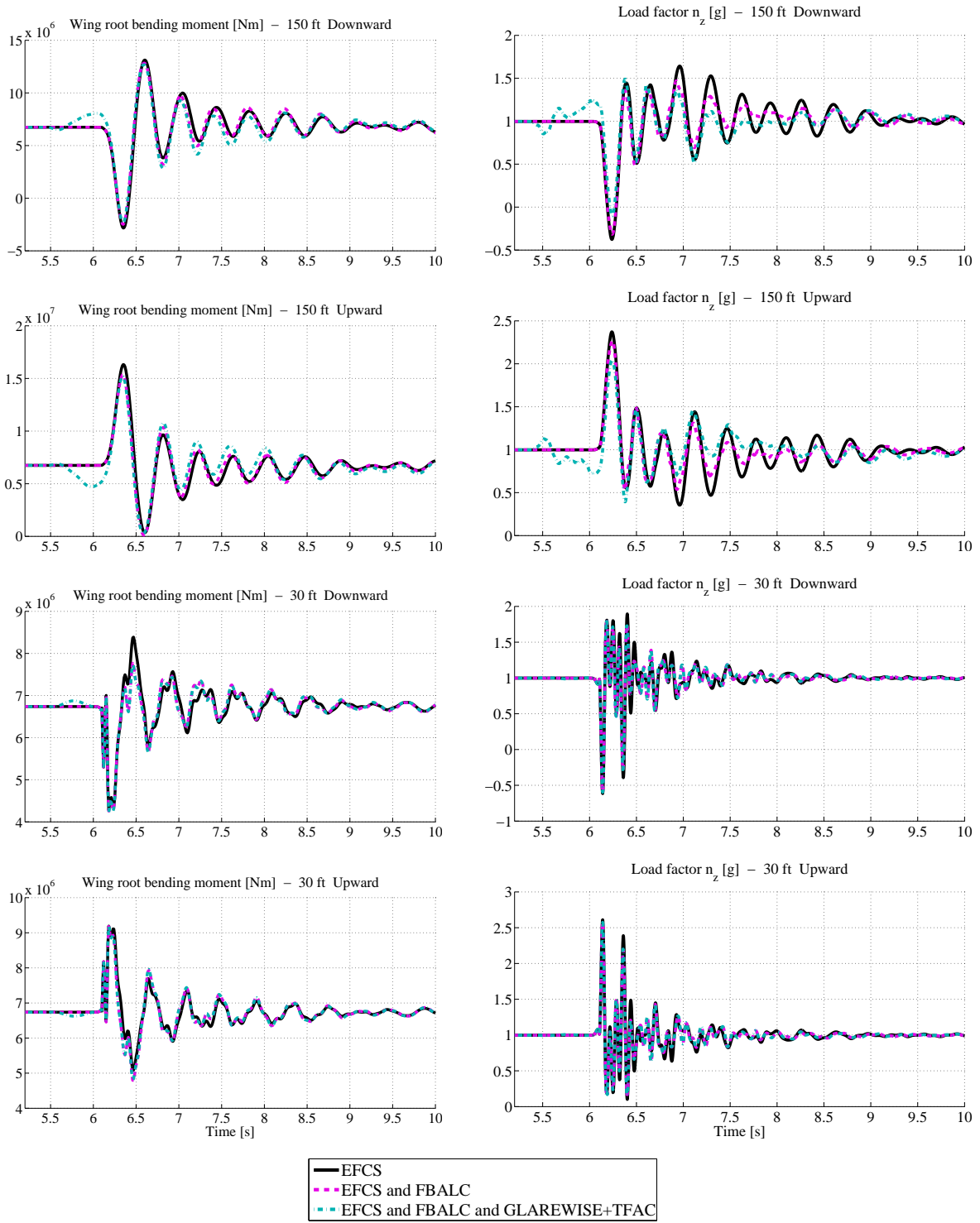
American Institute of Aeronautics and Astronautics

Figure 18. Comparison of wing root bending moments (left) and vertical acceleration at middle of cabin (right) over time during encounters with 1−cosine gusts of length 150 and 30 ft.

V.   Conclusions and Outlook

It was shown that both approaches proposed for the design of a feedback and of a feedforward gust load alleviation function are both practicable and meaningful. The general optimization-based design method described in section III was successfully applied to design feedback gust load alleviation systems. The full benchmark model (based on the XRF1 configuration provided by Airbus) includes, in addition to the aeroelastic model, a basis (rigid-body) flight control system. This complete nonlinear closed-loop model was used for the design of the load alleviation functions. No approximations have been necessary. Furthermore the control law designed contains nonlinearities like saturations and thresholds to avoid interaction with small command-induced accelerations and to avoid permanent actions of the surfaces. The presented FBALC was designed to reduce loads at the wing root. This could be achieved without increasing loads at other cut stations significantly. If more exact reference design loads are available, the figures in terms of load alleviation performance can be updated very quickly and a new tuning starting from the current solution can also be done.

The design approach is directly based on the various design objectives with which the domain specialists are used to work. This eases the comparison between several solutions as well as the design compromises. The execution time for one ordinary simulation to evaluate the criteria is about 12 minutes on a standard desktop PC, which is a rather long computation time for doing exhaustive optimizations. However, this shortcoming of the multi-objective simulation-based optimization can be attenuated by using the parallel computation features of the applied software. The LIDAR-based wind reconstruction algorithm behavior and performance (both reconstruction quality and speed) were well beyond all expectations at the beginning of the project. The results obtained by combining both functions FBALC and GLAREWISE+TFAC (see section IV.B) are very promising, even though still further investigations are needed to ensure that the best tuning and cooperation between these functions is achieved.

The work presented in this paper has brought significant progress for the maturation of such a combined feedback/feedforward load alleviation function. The potential for load alleviation is very promising. The gained experience and the developed tools (e.g. simulation models, LIDAR simulation, wind reconstruction algorithms) are pretty unique and shall serve as basis for further investigations. Overall, the proposed approach complements well the technology demonstrations that were performed during the European AW-IATOR project. Additional results (more cases and criteria) that were obtained with the presented load alleviation function can be found in Ref. 44. Further investigations on each function and on their integration are currently being performed within the Airframe-ITD part of the CleanSky 2 European aeronautics research initiative.

Acknowledgments

References

[1] Hargrove, W. J., "The C-5A Active Lift Distribution Control System," Tech. rep., NASA, 1976, N76-31148.

[2] Regan, C. D. and Jutte, C. V., "Survey of Applications of Active Control Technology for Gust Alleviation and New Challenges for Lighter-weight Aircraft," Tech. rep, TM-2012-216008, NASA, Dryden Flight Research Center, Edwards, CA, USA, April 2012.

[3] Hoffmann, G., "Stabilisierung, Böenkompensation und Schwingungsdämpfung am elastischen beweglichen Flugzeugmodell im Windkanal," Tech. rep., DFVLR (now part of DLR), Cologne, Germany, 1976.

[4] Krag, B., "The wind tunnel behaviour of a scaled model with a gust alleviation system in a deterministic gust field," *Transactions of the Institute of Measurement and Control*, Vol. 1, No. 3, July-September 1979.

[5] Böhret, H., Krag, B., and Skudridakis, J., "OLGA – An Open-Loop Gust Alleviation System," *Proceedings of the AGARD CP 384 Meeting*, Toronto, Canada, 1985.

⁶König, R. and Hahn, K.-U., "Load Alleviation and Ride Smoothing Investigations Using ATTAS," *Proceedings of the 17ᵗʰ Congress of the International Council of the Aeronautical Sciences*, Stockholm, Sweden, 1990.

⁷Hahn, K.-U. and König, R., "ATTAS Flight Test and Simulation Results of the Advanced Gust Management System LARS," *Proceedings of the AIAA Atmospheric Flight Mechanics Conference*, Hilton Head, SC, USA, 1992.

⁸König, R., Hahn, K.-U., and Winter, J., "Advanced Gust Management Systems - Lessons Learned and Perspectives," *Proceedings of the AGARD Flight Mechanics Panel Symposium on Active Control Technology: Applications and Lessons Learned*, Torino, Italy, 1994.

⁹Joos, H.-D., "Multi-Objective Parameter Synthesis (MOPS)," *Robust Flight Control: A Design Challenge*, edited by J.-F. Magni, S. Benani, and J. Terlouw, Vol. 224 of *Lecture notes in control and information sciences*, Springer, 1997, pp. 199–217.

¹⁰Joos, H.-D., "A Methodology for Multi-Objective Design Assessment and Flight Control Synthesis Tuning," *Aerospace Science and Technology*, Vol. 3, No. 3, 1999, pp. 161–176.

¹¹Joos, H.-D., Bals, J., Looye, G., Schnepper, K., and Varga, A., "A multi-objective optimisation based software environment for control systems design," *Proceedings of the 2002 IEEE International Conference on Control Applications and International Symposium on Computer Aided Control Systems Design (CCA/CACSD)*, Glasgow, Scotland, U.K., 2002.

¹²Joos, H.-D., "Worst Case Parameter Search Based Clearance Using Parallel Nonlinear Programming Methods," *Optimization Based Clearance of Flight Control Laws*, edited by A. Varga, A. Hansson, and G. Puyou, Vol. 416 of *Lecture Notes in Control and Information Science*, Springer, 2011.

¹³Looye, G., Joos, H.-D., and Willemsen, D., "Application of an Optimization-based Design Process for Robust Autoland Control Laws," *Proceedings of the AIAA Guidance, Navigation, and Control Conference and Exhibit*, Montreal, Canada, August 2001.

¹⁴Looye, G. and Joos, H.-D., "Design of Robust Dynamic Inversion Control Laws using Multi-Objective Optimization," *Proceedings of the AIAA Guidance, Navigation, and Control Conference and Exhibit*, Montreal, Canada, August 2001, AIAA-2001-4285.

¹⁵Hecker, S. and Hahn, K.-U., "Gust Computation System," Tech. rep., DLR, Oberpfaffenhofen, Germany, May 2003, AWIATOR, Technical Report, DLR-TR-3.1.1-11.

¹⁶Hahn, K.-U. and Hecker, S., "Gust Load Alleviation System," Tech. rep., DLR, Braunschweig, Germany, April 2004, AWIATOR, Technical Report, DLR-TR-3.1.1-12.

¹⁷Hecker, S., "Proposal of gust load alleviation system using adaptive elements," Tech. rep., DLR, Oberpfaffenhofen, Germany, 2005, AWIATOR, Technical Report, DLR-TR-3.1.1-13.

¹⁸Hecker, S. and Hahn, K.-U., "Proposal of gust load alleviation system using turbulence sensor and adaptive elements," Tech. rep., DLR, Oberpfaffenhofen, Germany, July 2006, AWIATOR, Technical Report, DLR-TR-3.1.1-14.

¹⁹Schmitt, N. P., Rehm, W., Pistner, T., Zeller, P., Reithmeier, G., Stilkerich, S., Schertler, K., Diehl, H., and Zinner, H., "The AWIATOR Airborne LIDAR Turbulence Sensor," *Proceedings of the 2005 German Aerospace Congress (Deutscher Luft- und Raumfahrtkongress / DLRK)*, Friedrichshafen, Germany, 26-29 September 2005, DGLR-2005-067.

²⁰Rabadan, G. J., Schmitt, N. P., Pistner, T., and Rehm, W., "Airborne Lidar for Automatic Feedforward Control of Turbulent In-Flight Phenomena," *Journal of Aircraft*, Vol. 47, No. 2, March-April 2010, pp. 392–403.

²¹Kordt, M., Ballauf, C., and Joos, H.-D., "Load alleviation for large aeroplanes by active mode control of the coplanar motion of the horizontal tailplane," *Proceedings of IFASD International Forum on Aeroelasticity and Structural Dynamics*, Madrid, Spain, June 2001.

²²Jeanneau, M., Aversa, N., Delannoy, S., and Hockenhull, M., "AWIATOR's Study of a Wing Load Control: Design and Flight–Test Results," *Proceedings of the 16ᵗʰ IFAC Symposium on Automatic Control in Aerospace*, Saint-Petersburg, Russia, 2004.

²³Cézard, N., Besson, C., Dolfi-Bouteyre, A., and Lombard, L., "Airflow Characterization by Rayleigh-Mie Lidars," *AerospaceLab*, Vol. 1, December 2009, pp. 1–4.

²⁴Herbst, J. and Vrancken, P., "Design of a monolithic Michelson interferometer for fring imaging in a near-field, UV, direct-detection Doppler wind lidar," *Applied Optics*, Vol. 55, No. 25, September 2016, pp. 6910–6929.

²⁵Hill, C. and Harris, M., "Lidar measurement report," Tech. rep., QinetiQ, September 2010, Technical report: Remote Sensing (UpWind WP6) – QinetiQ Lidar Measurement Report, (QINETIQ/ TS/ FPPS/ TR0900813).

²⁶Wolkensinger, C., "Vergleich messtechnischer Konzepte zur bordgestützten Ermittlung atmosphärischer Störphänomene," DLR report DLR-IB-111-2010/35, DLR, Institute of Flight Systems, Braunschweig, Germany, 2010.

²⁷Hirschberger, M. C., *Beiträge zur Erfassung von Wirbelschleppen mit Lidar - Simulation und Analyse rückgestreuter Signale zur Windfeldbestimmung vor Flugzeugen*, Ph.D. thesis, Ludwig–Maximilians-Universität, Munich, Germany, 2013.

²⁸Barbaresco, F., "Airport radar monitoring of wake vortex in all weather conditions," *European Radar Conference (EuRAD)*, 2010, pp. 85–88.

²⁹Barbaresco, F. and Meier, U., "Radar monitoring of a wake vortex: Electromagnetic reflection of wake turbulence in clear air," *Comptes Rendus Physique*, Vol. 11, No. 1, 2010, pp. 54–67.

³⁰Neece, R. T., Britt, C. L., White, J. H., Mudukutore, A., Nguyen, C., and Hooper, B., "Wake Vortex Tracking Using a 35 GHz Pulsed Doppler Radar," *Proceedings of the 5ᵗʰ NASA Integrated Communications, Navigation, and Surveillance (ICNS) Conference and Workshop*, Fairfax, VA, USA, 2-5 May 2005.

³¹Ehlers, J. and Fezans, N., "Airborne Doppler LiDAR Sensor Parameter Analysis for Wake Vortex Impact Alleviation Purposes," *Advances in Aerospace Guidance, Navigation and Control*, edited by J. Bordeneuve-Guibé, A. Drouin, and C. Roos, Springer, 2015, pp. 433–453.

³²Fezans, N., Schwithal, J., and Fischenberg, D., "In-Flight Remote Sensing and Characterization of Gusts, Turbulence, and Wake Vortices," *Proceedings of the 2015 German Aerospace Congress (DLRK 2015)*, Rostock, Germany, September 2015.

³³Gerz, T., Holzäpfel, F., and Darracq, D., "Commercial aircraft wake vortices," *Progress in Aerospace Sciences*, Vol. 38, 2002, pp. 181–208.

[34] Luckner, R., "Modeling and Simulation of Wake Vortex Encounters: State-of-the-Art and Challenges," *Proceedings of the AIAA Modeling and Simulation Technologies Conference*, Minneapolis, MN, USA, August 2012, AIAA-2012-4633.

[35] Ehlers, J., Fischenberg, D., and Niedermeier, D., "Wake Identification Based Wake Impact Alleviation Control," *Proceedings of the 14th AIAA Aviation Technology, Integration, and Operations Conference*, Atlanta, GA, USA, June 2014, AIAA-2014-2591.

[36] Sivia, D. S., *Data Analysis - A Bayesian Tutorial*, Oxford University Press, 2nd ed., July 2006, ISBN-13: 978-0198568315.

[37] Gregory, P., *Bayesian Logical Data Analysis for the Physical Sciences*, Cambridge University Press, 2005, ISBN-13: 978-0-521-84150-4.

[38] Fezans, N., Schwithal, J., and Fischenberg, D., "In-flight remote sensing and characterization of gusts, turbulence, and wake vortices," *Proceedings of the 2015 German Aerospace Congress (Deutscher Luft- und Raumfahrtkongress)*, Rostock, Germany, September 2015.

[39] Fezans, N., Schwithal, J., and Fischenberg, D., "In-flight remote sensing and identification of gusts, turbulence, and wake vortices using a Doppler LIDAR," *CEAS Aeronautical Journal*, March 2017, doi:10.1007/s13272-017-0240-9.

[40] Fraley, C., "Algorithms for Nonlinear Least-Squares Problems," Tech. rep., ADA196071, DTIC, May 1988.

[41] Tikhonov, A. N. and Arsenin, V. Y., *Solutions of Ill-Posed Problems*, Winston and Sons, Washington, DC, USA, 1977.

[42] Tikhonov, A. N., Goncharsky, A., Stepanov, V. V., and Yagola, A. G., *Numerical Methods for the Solution of Ill-Posed Problems*, Springer-Science+Business Media, B.V., Dordrecht, The Netherlands, 1995, ISBN-13: 978-0-7923-3583-2.

[43] Marr, D. and Hildreth, E., "Theory of Edge Detection," *Proceedings of the Royal Society of London. Series B, Biological Sciences*, Vol. 207, No. 1167, February 1980, pp. 187–217.

[44] Fezans, N. and Joos, H.-D., "Integrated active gust and turbulence load alleviation functions," Tech. rep., DLR-IB-111-2014/51 - CleanSky SFWA OP1.2.3-25, DLR, Germany, 2014.

[45] Mallat, S., *A Wavelet Tour of Signal Processing - The Sparse Way*, Academic Press, 2009, ISBN: 978-0-12-374370-1.

[46] Addison, P. S., *The Illustrated Wavelet Transform Handbook - Introductory Theory and Applications in Science, Engineering, Medicine and Finance*, CRC Press, 2nd ed., 2016, ISBN: 978-1-4822-5132-6.

[47] Deiler, C., "Data parser approaches for (online) parameter estimation," *CEAS Aeronautical Journal*, Vol. 5, No. 3, 2014, pp. 345–357.

[48] Fezans, N., "An Unusual Structure for a Feedforward Gust Load Alleviation Controller," *Proceedings of the 2017 CEAS EuroGNC Conference*, Warsaw, Poland, April 2017.

[49] Atto, A. M., Pastor, D., and Mercier, G., "Smooth sigmoid wavelet shrinkage for non-parametric estimation," *Proceedings of the 2008 IEEE International Conference on Acoustics, Speech, and Signal Processing (ICASSP)*, Las Vegas, NV, USA, 2008.

[50] Atto, A. M., Pastor, D., and Mercier, G., "Wavelet shrinkage: unification of basic thresholding functions and thresholds," *Signal, Image and Video Processing (SIViP)*, Vol. 5, No. 1, March 2008, pp. 11–28, DOI 10.1007/s11760-009-0139-y.

[51] Lorenz, D. A., *Wavelet Shrinkage in Signal & Image Processing*, Ph.D. thesis, University of Bremen, Bremen, Germany, October 2004.

[52] Looye, G. and Leitner, M., "XRF1 Model Guide," Tech. rep., CleanSky SFWA-ITD D1.2.4.3-5, DLR, Oberpfaffenhofen, Germany, June 2013.

[53] Kubica, F. and Madelaine, B., "Passenger comfort improvement by integrated control law design," *Proceedings of the RTO AVT Specialists' Meeting on "Structural Aspects of Flexible Aircraft Control"*, Ottawa, Canada, October 1999.

[54] "ISO 2631-1:1997: Mechanical vibration and shock – Evaluation of human exposure to whole-body vibration – Part 1: General requirements," May 1997.